ETH
Eidgenössische Technische Hochschule Zürich
Swiss Federal Institute of Technology Zurich

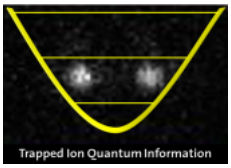

ETH Zürich, Departement of Physics

Focused Raman Beam Addressing for a Trapped-Ion Quantum Processor

Master Thesis

Supervisors:
Dr. Daniel Kienzler
Prof. Dr. Jonathan Home

Student:
Manuel Zeyen

April 2016

Abstract

The ongoing miniaturization of technology drives the development of methods for quantum information processing. The long-term goal is a machine performing calculations based on the laws of quantum mechanics. Currently the limiting factor is reliable multi-qubit gate operation. Single and two-qubit gates using trapped ions reach the highest fidelities to date, close to the threshold required for fault tolerant computation. Thus the focus is gradually shifting from increasing fidelity to scaling up the number of qubits available for quantum information processing tasks.

This master's thesis contributes to the solution of both issues. An optical system theoretically capable of focusing both 397 and 401 nm light to a spot size below 1.3 µm was designed and a prototype set up. Using 397 nm light, trapped $^{40}Ca^{+}$ ions in a chain will be addressed individually for either qubit Raman-transitions or individual read-out. Using 401 nm will enable individual AC-Stark shifting of trapped ions, away from their qubit transition. During this project, the imaging system used in the lab was confirmed to be near diffraction limited and high quality imaging of ions was achieved.

In a second project, a laser diode at 397 nm was optically injection locked to emit 130mW of optical power around 377.6114 THz with 500 KHz linewidth. Amplitude modulation of the seed light in a range of 3 MHz around the carrier was not significantly suppressed by the injected diode. This stands in contrast to what previous results in the infrared regime suggested. A seed light power threshold required for clean diode injection was observed, limiting the locking time of the injected diode to 20 ns. The injection locked light of the diode could be separated spatially from its free running output, promising applications in the scaling of ion trap experiments.

Acknowledgements

First of all, I would like to thank Prof. Jonathan Home for giving me the opportunity to trap ions in his group. The project was extensive and touched many aspects in the lab, which was at the same time challenging and very rewarding. Jonathan's unshakable optimism is contagious.

I then want to thank Dr. Daniel Kienzler for supervising me, answering all my questions and showing me valuable tricks in the lab. It was great, learning from the trap-builder himself. Many thanks to Dr. Hsiang-Yu Lo, who supervised the last month of my project. I would like to thank all members of the TIQI lab for helping me with all the small problems that arise in such a hands-on project. It was a pleasure working with all of you.

I want to thank my family for their unconditional love and my brother for the cakes. Last but not least I thank Carmen, who showed great patience and sometimes even understanding when the lab had its own mind.

Contents

General Introduction

The Trapped Ion Quantum Information (TIQI) laboratory at ETH Zürich is pursuing precision control over trapped ions in order to understand the loss of coherence in quantum systems. Simultaneously, new trap designs, methods of quantum information processing as well as quantum state generation and manipulation are developed. One of the ion species found in the TIQI lab is $^{40}Ca^{+}$. Optical wavelengths are used for the experiments and this work will deal in particular with blue laser light at 397 nm. This master's thesis is developing two systems improving the control of trapped ions and related experiments.

The first project involved frequency stabilization of a laser diode at 397 nm by optically injection locking it to a laser with 500 KHz linewidth. The second project aimed at optical addressing of a single ion in a trapped ion chain. An already installed imaging system was upgraded in order to use it as a addressing system able to focus laser light of 397 and 401 nm down to 1 µm spot size.

As both projects have only the wavelength of the involved laser light as common ground, this thesis is separated into two parts. The first part describes optical injection locking and two follow-up projects investigating its dynamic processes. The second part describes the development and installing of a lens system capable of focusing light on a single trapped ion.

Part I

Optical Injection Locking of a 397 nm Laser Diode

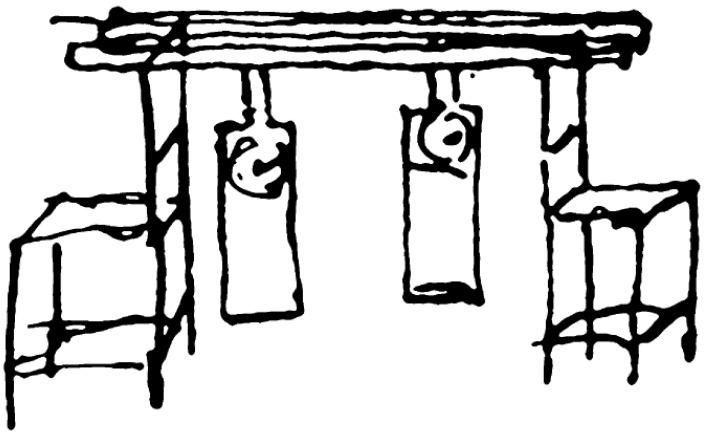

Huygens original drawing from 1665 showing two synchronized pendulum clocks on a common support. Credit: [3]

Chapter 1

Introduction

"*If one synchronized swimmer drowns, do the rest drown too?*"
— George Carlin

A constant concern in atomic physics experiments is laser power. At the moment, the TIQI lab has limited power at 397 nm wavelength and different setups have to share it amongst each other. Especially non-resonant processes rely on sufficient laser power. The TIQI lab plans for example to use the two $4S_{1/2}$ Zeeman states of $^{40}Ca^{+}$ as qubits [1], coupled by a Raman transition. The higher the laser power, the faster the transition will be driven thereby minimizing decoherence. The first part of this master's thesis is concerned with setting up an optically injection locked 397 nm laser diode, as the first of potentially several high power laser sources in the lab at this wavelength.

The freely emitting laser diode produced a maximal optical power of 140 mW at 150 mA drive current. In most cases, modern quantum mechanical experiments require lasers of spectral purity, which is difficult to achieve at such high powers. There is however a way to force the high power laser to oscillate exactly at the frequency dictated by a very well controlled low power laser. Already in 1665 Christiaan Huygens noticed, that two pendulums of different clocks hung up on the same wall, fell invariably in synchrony. After hanging them on different walls, no synchrony was observed. He explained the synchronization of the clocks with vibrations transmitted through the wall from clock to clock. In modern language, one of the two oscillators was locked by injection to the other. Injection locking can happen in virtually any type of coupled oscillator system such as radio frequency controlled clocks, cardiac pacemakers or even the 24h day-night rhythm of human beings. A laser can be viewed as a radiatively fed-back high frequency oscillator, and in this case one talks about optical injection locking. A nice overview of the development of this field can be found in [2]. A very good book on injection locking and oscillator synchrony in general is "Synchronization - A Universal Concept in Nonlinear Sciences" by Pikovsky, Rosenblum and Kurths [3].

On a fundamental level, injection locking means that a system oscillating at angular frequency ω_1 close to the resonance frequency ω_2 of a second system, can force the second system to oscillate at ω_1 and suppress all oscillation at ω_2. Since the signal originally oscillating at ω_2 is totally controlled by the locking signal, we call it the "master" and the injected oscillator the "slave". In the TIQI lab, a laser is locked to precisely $\omega_1 = 2\pi \cdot 377.6114$ THz (corresponding to 793.9179 nm). After frequency doubling it, we use it as the master laser, to force the slave high

power laser diode to emit precisely at the master-frequency.

Having a precisely controlled high power laser source benefits the TIQI lab in two ways. The first is of practical nature. Setting up a high power 397 nm source at the location where it is needed, no longer requires transmitting lots of power through optical fibers. We noticed the slow degradation of the spatial mode profile of high intensity beams output from fibers, which we suspect is due to dirty fiber tips. One possibility is that the high intensity at the fiber tip acts as a dipole trap for dust and oil particles in the air. The second benefit is the high power requirement for electromagnetically induced transparency (EIT) cooling. EIT cooling is based on an off resonant two photon process, which is greatly improved by higher laser power [4].

Apart from optically injecting a laser diode, this master's thesis investigated dynamical processes in the diode as well. The first project investigated the ability of the diode to filter out frequency componenets in the master light. In the TIQI lab, unwanted frequency components in the 397 nm laser hurt the ion trapping experiments [6]. We thus investigated the possibility of filtering out theses frequencies via injection locking. Spectral filtering of the slave output has been achieved previously [7], and the filtering of master light by optical injection locking was investigated in the infra-red domain [2]. The present master's thesis combines both experiments in the UV region. The second project, was to spatially separate injected from non-injected light using a diffraction grating and measure the frequency settling time of the injected slave diode. Usually laser light is first frequency stabilized and switched before hitting the ions. In my experiment, the switching of the stabilization mechanism itself was investigated, potentially helping to further increase the scalability of ion trapping experiments.

The outline of this part of the thesis is as follows. Chapter 2, introduces the theory of injection locking, in order to understand the time dependent behavior of injection locking. Chapter 3 explains how we were able to characterize the quality of our injection, and finally Chapter 4 presents the results of the filtering and switching experiments.

Chapter 2

Optical Injection Locking Theory

2.1 Qualitative Description

This section, gives a qualitative derivation how a high power laser can be forced into synchrony with a low power laser. An intuitive argument is given, why for example a red laser cannot be injection locked by a blue laser, that is to say, a range of frequencies is given around the frequency of the strong laser, for which injection locking is possible.

In order to synchronize two oscillators, information has to be exchanged in one way or another. For lasers, the easiest way is simply to shine an external laser beam of intensity I_{inj} oscillating at ω_{inj} directly into a laser cavity, running freely with stable intensity output I_{free} at frequency ω_{free}. The laser cavity is composed of two mirrors as can be seen in Figure 2.1.1 a), where we assume for simplicity that mirror 1 has reflection $R_1 = 1$ (corresponding to 100% reflection), and mirror 2 has reflectivity R. The three involved time dependent fields are the injected field $E_{\text{inj}}(t)$, the circulating field $\tilde{E}_{\text{cav}}(t)$ reflected by the mirrors and the outcoupled field $E(t)$ which will all be described further in Section 2.2. Between the two cavity mirrors is placed a material, amplifying some of the modes of $\tilde{E}_{\text{cav}}(t)$. Which modes are amplified, is specified by the gain function of the material sketched in Figure 2.1.1 b). This function can be complex, and in the high gain limit expressed as (see [8])

$$g(\omega) \approx \frac{1-R}{1-G+iGT(\omega-\omega_{\text{free}})} \tag{2.1.1}$$

where T is the time for one round trip in the cavity, G the total round-trip gain magnitude and ω_{free} the resonance frequency. For $G \approx 1$, eq. (2.1.1) is simplified further to

$$|g(\omega)|^2 \approx \frac{(1-R)^2/T^2}{(\omega-\omega_{\text{free}})^2} \equiv \frac{\gamma_{\text{out}}^2}{(\omega-\omega_{\text{free}})^2} \tag{2.1.2}$$

with external cavity loss rate $\gamma_{\text{out}} = (1-R)/T = \omega/Q$ and Q the quality factor of the laser cavity. The intensity $I_{\text{out}} = |E_{\text{out}}|^2$ of the output field is then

$$I_{\text{output}} = I_{\text{signal}}|g(\omega)|^2. \tag{2.1.3}$$

The free running laser cavity in its equilibrium state has an output intensity of I_{free}. As a crude condition on when the injected signal intensity starts to influence the laser cavity (see

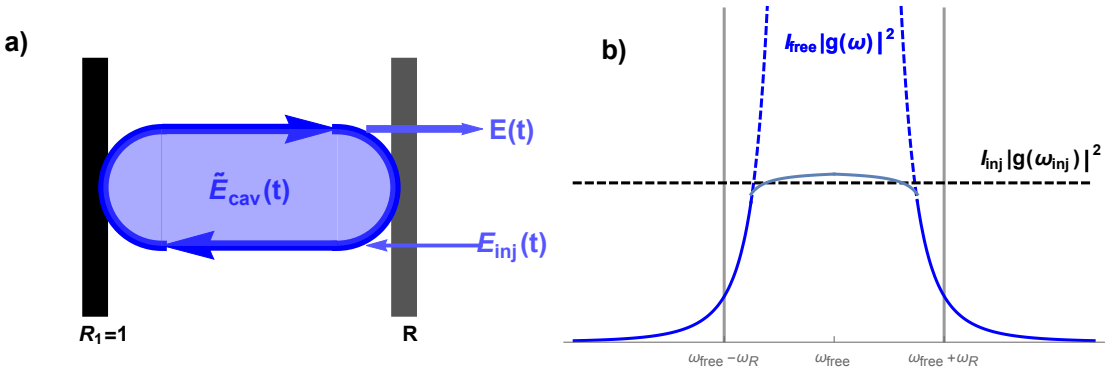

Figure 2.1.1: **a**) Sketch of the laser cavity with the injected field $E_{\text{inj}}(t)$, the circulating field $\tilde{E}_{\text{cav}}(t)$ and the outcoupled field $E(t)$. **b**) Gain profile of a free running (dashed) or injected (solid) laser.

Figure 2.1.1), the amplified I_{inj} and the free running signal intensity are equated:

$$I_{\text{free}} \approx I_{\text{inj}}|g(\omega_{\text{inj}})|^2 = I_{\text{inj}}\frac{\gamma_{\text{out}}^2}{(\omega_{\text{inj}}-\omega_{\text{free}})^2}. \tag{2.1.4}$$

Solving (2.1.4) for the frequency difference, gives

$$\omega_{\text{R}} \equiv |\omega_{\text{inj}}-\omega_{\text{free}}| \approx \gamma_{\text{out}}\sqrt{\frac{I_{\text{inj}}}{I_{\text{free}}}} = \frac{\omega_{\text{free}}}{Q}\sqrt{\frac{I_{\text{inj}}}{I_{\text{free}}}}. \tag{2.1.5}$$

This can be taken as rough boundary for the detuning between master and slave laser. Already from this short derivation, one sees, that the injection depends on the square root of the ratio of the two laser powers (intensity is power over illuminated area) and the decay rate of the laser cavity (or its quality factor). But since time dependents of injection locking are investigated too in Section 4.2, a better understanding of the dynamics underlying injection locking is developed in the following section. Laser oscillator equations leading to the Adler equation will enable the discussion of the sudden turn on of the injecting master laser.

2.2 Adler Equation

2.2.1 Basic Laser Oscillator Equations

The Adler equation is presented here from the point of view of laser physics. In 1946 Adler derived an equation describing the phase locking mechanism of electronic LC oscillator circuits [11], and it was later found that his equation could equally well describe the locking of laser oscillators [12].

Following [8] the injected electric field amplitude from Section 2.1 can be written as

$$E_{\text{inj}}(t) = \mathcal{E}_{\text{inj}}(t)e^{i(\omega_{\text{inj}}t+\phi_{\text{inj}}(t))} \tag{2.2.1}$$

with $\mathcal{E}_{\text{inj}}$ the injected field amplitude and $\phi_{\text{inj}}(t)$ keeping track of additional phase variations if needed. The injected field intensity is simply $I_{\text{inj}}(t) = |E_{\text{inj}}(t)|^2$. The field $E_{\text{inj}}(t)$ inside the cavity is given by

$$E_{\text{cav}}(t) = \mathcal{E}_{\text{cav}}(t)e^{i(\omega_{\text{inj}}t+\phi(t))} \tag{2.2.2}$$

where $\phi(t)$ introduces the appropriate phase variation if it freely oscillates not at ω_{inj} but at a different ω_{free}. In the simplest case $\phi(t) = (\omega_{\text{free}} - \omega_{\text{inj}})\, t - \phi_{\text{inj}}(t)$. The complete derivation of the following laser-oscillator-equations is beyond the scope of this work and can be found in [8]. The amplitude and phase equations of the output field $E(t)$ with amplitude $\mathcal{E}(t)$ yield

$$\frac{d\mathcal{E}(t)}{dt} + \frac{\gamma_{\text{cav}} - \gamma_{\text{grow}}}{2} E(t) = \gamma_{\text{out}} \mathcal{E}_{\text{inj}}(t) \cos(\phi(t) - \phi_{\text{inj}}(t)) \tag{2.2.3}$$

$$\frac{d\phi(t)}{dt} + \omega_{\text{inj}} - \omega_{\text{free}} = -\gamma_{\text{out}} \frac{\mathcal{E}_{\text{inj}}(t)}{\mathcal{E}(t)} \sin(\phi(t) - \phi_{\text{inj}}(t)) \tag{2.2.4}$$

where γ_{cav} stands for the cavity loss rate and γ_{grow} for the growth rate.

2.2.2 The Steady-State Solution

With equations (2.2.3) and (2.2.4) at hand, the steady-state behavior of an injected laser oscillator can be found. For weak steady state injected laser fields $\mathcal{E}_{\text{inj}}(t) \ll \mathcal{E}(t)$ holds. For simplicity, $\phi_{\text{inj}}(t) = \phi(0)$ is kept constant, so phase noise of the master is neglected. The amplitude equation is not particularly insightful. The cavity output amplitude will almost stay constant $\mathcal{E}(t) \approx \mathcal{E}_{\text{SS}}$ and γ_{grow} is saturated down to γ_{cav}. The resulting steady-state equation

$$\frac{\gamma_{\text{cav}} - \gamma_{\text{grow}}}{2} = \gamma_{\text{out}} \frac{\mathcal{E}_{\text{inj}}}{\mathcal{E}} \cos(\phi(t) - \phi(0)) \tag{2.2.5}$$

is therefore always satisfied with both sides approximately zero.

The phase equation (2.2.4) is much more insightful. In the steady-state, it reduces to

$$\omega_{\text{inj}} - \omega_{\text{free}} + \gamma_{\text{out}} \frac{\mathcal{E}_{\text{inj}}}{\mathcal{E}} \sin(\phi(t) - \phi(0)) = 0 \tag{2.2.6}$$

where we identify $\gamma_{\text{out}} \frac{\mathcal{E}_{\text{inj}}}{\mathcal{E}}$ with ω_{R} from (2.1.5) as the field amplitude is the square root of the intensity. Solving for $\phi(t)$ simply yields

$$\phi(t) = \arcsin\left(\frac{\omega_{\text{free}} - \omega_{\text{inj}}}{\omega_{\text{R}}}\right) + \phi(0) \tag{2.2.7}$$

which gives the steady state phase difference between the initial phase of the free running oscillator and the injected signal phase. This phase depends on the locking range and, as will be see in Section 2.3, governs the transient behavior of injection locking. Before starting this discussion, note that (2.2.6) leads to exactly the same locking range we already encountered. The fact that $\sin(x)$ is bounded by -1 and 1 immediately gives

$$-\gamma_{\text{out}} \frac{\mathcal{E}_{\text{inj}}}{\mathcal{E}} = -\omega_{\text{R}} \leq \omega_{\text{free}} - \omega_{\text{inj}} \leq +\omega_{\text{R}} = \gamma_{\text{out}} \frac{\mathcal{E}_{\text{inj}}}{\mathcal{E}} \tag{2.2.8}$$

which for the total allowed frequency range $\Delta\omega = 2\omega_{\text{R}}$ is the same result we derived earlier. To summarize, a laser oscillating with frequency ω_{free} can be locked to another laser at frequency ω_{inj}, if $|\omega_{\text{free}} - \omega_{\text{inj}}| \lesssim \omega_{\text{R}}$. Frequencies ω_{inj} and ω_{free} are said to be close to each other, if both satisfy this relation.

2.3 Time Dependent Injection

2.3.1 Solving the Adler Equation

With an equation describing the time dependence of the slave signal phase, the sudden turn on of the master signal can be investigated. Here, the focus is on the case, where the slave laser is stable and a perturbing injecting signal is suddenly applied as a square wave. This process is called pulsed injection[1]. Detailed analysis of static as well as dynamic processes in optical injection locking of semiconductor laser diodes has been performed in e.g. [13, 14], but in-depth analysis is beyond the scope of the present work. To give the basic concepts, below is given an intuitive way of tackling time dependent injection locking, based on the Adler equation.

It will later be seen that the fast frequency change of the slave laser by switching the master laser can be checked with a diffraction grating, which separates the free running slave light spatially from the injected master light. The goal of this section is therefore to derive an equation, for the instantaneous frequency of the slave.

First of all, remember that two oscillators with a constant phase relation have the same frequency. This means the settling time t_∞ of the phase difference between the slave and the master has to be found. In a coordinate system rotating at ω_{inj} and if the master has a constant phase $\phi(0)$, the instantaneous phase difference between master and slave is

$$\phi(t) = \omega_{\text{osc}}(t)t - \phi(0)$$

with $\omega_{\text{osc}}(t)$ being the instantaneous frequency of the slave and no longer its free running ω_{free}. The value where this phase difference settles will be denoted as

$$\phi(t_\infty) \approx \phi(\infty) \equiv \phi_\infty. \tag{2.3.1}$$

Second, the time derivative of the phase of an oscillator is simply its instantaneous angular frequency. Since the initial frequency of the slave is its free running frequency,

$$\omega_{\text{osc}}(t) = \omega_{\text{free}} + \frac{d\phi(t)}{dt} \tag{2.3.2}$$

holds at every time step. If ω_{inj} is well inside the locking range (2.1.5), we will also have $\lim_{t\to\infty} \omega_{\text{osc}}(t) = \omega_{\text{inj}}$. Adler's equation

$$\frac{d\phi(t)}{dt} = (\omega_{\text{free}} - \omega_{\text{inj}}) - \omega_{\text{R}} \sin(\phi(t) - \phi(0)) \tag{2.3.3}$$

describes the instantaneous phase difference between master and slave, not the frequency. So an analytical solution for the phase has to be found, and its time derivative taken. The analytical solution is given by (see Appendix A)

$$\tan\left(\frac{\phi(t) - \phi(0)}{2}\right) = \frac{\omega_{\text{L}}}{\omega_{\text{free}} - \omega_{\text{inj}}} - \frac{\omega_{\text{R}}}{\omega_{\text{free}} - \omega_{\text{inj}}} \tanh\left(\frac{\omega_{\text{R}}(t - t_0)}{2}\right) \tag{2.3.4}$$

with $\omega_{\text{L}} = \sqrt{\omega_{\text{R}}^2 - (\omega_{\text{free}} - \omega_{\text{inj}})^2}$, the geometric mean between $\omega_{\text{free}} - \omega_{\text{inj}} + \omega_{\text{R}}$ and $\omega_{\text{free}} - \omega_{\text{inj}} - \omega_{\text{R}}$. As can be seen from Figure 2.3.1, the important feature of this complicated expression is

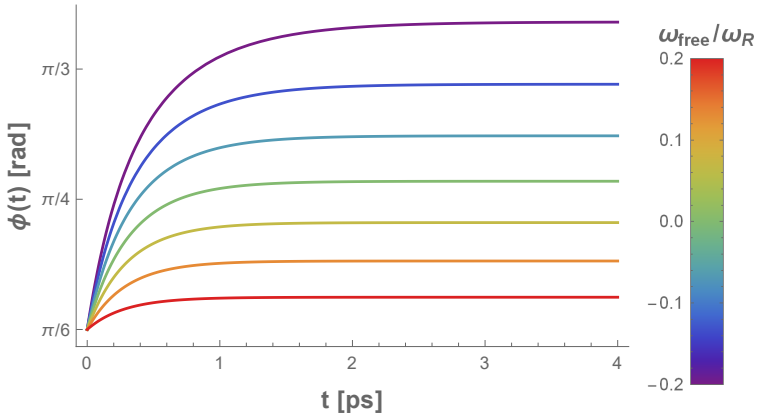

Figure 2.3.1: Simulated transient phase locking for different ω_{free} inside the locking range. The initial phase difference $\phi(0)$ was fixed at $\pi/6$, all other parameters are kept fixed at experimental values given in table 2.3.1.

the fact that it settles for all ω_{free} inside the locking range. Adler's equation (2.2.4) has two steady state solutions given by

$$\phi_\infty = \arcsin\left(\frac{\omega_{\text{free}} - \omega_{\text{inj}}}{\omega_{\text{R}}}\right) \tag{2.3.5}$$

$$\phi_\infty^{\text{unstable}} = \pi - \arcsin\left(\frac{\omega_{\text{free}} - \omega_{\text{inj}}}{\omega_{\text{R}}}\right) \tag{2.3.6}$$

where only ϕ_∞ is reached smoothly by $\phi(t)$. In contrast, $\phi_\infty^{\text{unstable}}$ is only attained, if $\phi(0)$ has had this value from the beginning. Realistic oscillators are subject to phase noise, so $\phi(t) \neq \phi_\infty^{\text{unstable}}$ after a short period of time after which $\phi(t)$ will smoothly settle on ϕ_∞. This behavior is very well described by the diagram in Figure 2.3.2 (see [8, 9]). The stable and unstable solutions are immediately spotted and in addition the locking range as well as the effect of different initial detuning $\omega_{\text{free}} - \omega_{\text{inj}}$ is easily read off .

One question remains: How long does the frequency locking actually take?

2.3.2 Time Dependence

To understand the transient frequency evolution qualitatively, the transient phase response given by eq. (2.3.4) is first linearized for the case $|\phi_\infty - \phi(0)| \ll \pi$. So the special case of a small initial phase lag with respect to the settling phase is treated. For simplicity, the starting point of the injecting signal is defined at $t_0 = 0$. Taylor expansion results in

$$\tan\left(\frac{\phi(t)}{2}\right) = \phi_\infty + \left(\tan\left(\frac{\phi(0)}{2}\right) - \phi_\infty\right) e^{-\omega_{\text{R}} t}. \tag{2.3.7}$$

[1] For the opposite case, where the master laser is continuous wave and the slave laser gain is suddenly turned up, instead of being locked, the slave frequency is merely pulled to the master frequency (see [8, 9, 10]). This is sometimes erroneously called pulsed injection as well, but in reality should be called pulsed seeding.

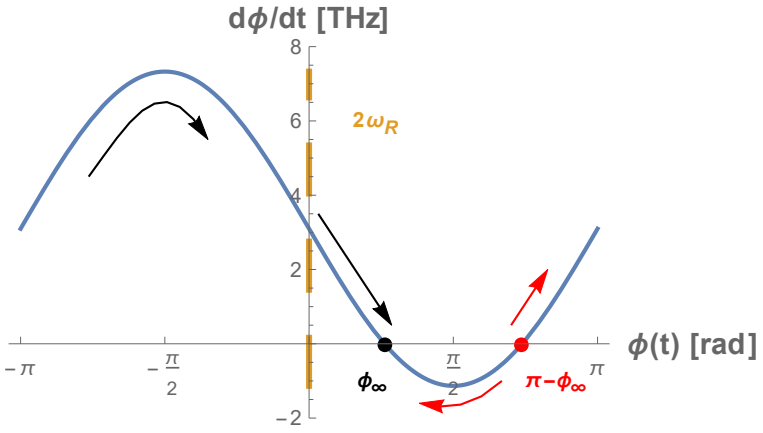

Figure 2.3.2: Diagram of Adler's equation 2.3.3. The stable steady state solution is ϕ_∞ (black), the unstable one is $\pi - \phi_\infty$ (red). The arrows indicate in which direction the phase $\phi(t)$ will evolve. Twice the locking range corresponds to the amplitude (orange line). A phase offset shifts the sine wave horizontally, whereas a different detuning $\omega_{\text{free}} - \omega_{\text{inj}}$ shifts it vertically. For a detuning larger than the locking range, no steady state solution is found.

If $|\omega_{\text{free}} - \omega_{\text{inj}}| \ll \omega_{\text{R}}$ and $\phi(0)$, $\phi_\infty \ll 1$ holds, eq. (2.3.7) can be simplified further to

$$\phi(t) \approx 2\phi_\infty + (\phi(0) - 2\phi_\infty)\, e^{-\omega_{\text{R}} t} \tag{2.3.8}$$

with the obvious locking time scale

$$t_{\text{lock}} \approx \frac{1}{\omega_{\text{R}}}. \tag{2.3.9}$$

For optical frequencies, ω_{R} lies in the THz regime, so locking should happen extremely fast (in the range of picoseconds).

Calculating the locking time more precisely, requires an expression for the instantaneous frequency. Following [9] and using eq. (2.3.2) and eq. (2.3.3) one gets

$$\omega_{\text{osc}}(t) = \omega_{\text{free}} - \frac{\omega_{\text{R}}^2}{(\omega_{\text{free}} - \omega_{\text{inj}})} \frac{\operatorname{sech}^2(\omega_{\text{R}} t/2)}{1 + \left(\frac{\omega_{\text{L}} - \omega_{\text{R}} \tanh(\omega_{\text{R}} t/2)}{\omega_{\text{free}} - \omega_{\text{inj}}}\right)^2}. \tag{2.3.10}$$

The locking time t_{lock} is then defined as the time it takes for the slave frequency to settle within 0.1% of the final value ω_{inj} (to which it always converges), and obtained by simply solving

$$0.001\omega_{\text{inj}} = \omega_{\text{osc}}(t). \tag{2.3.11}$$

Equation (2.3.10) might suggest, that two parameters are important: the initial detuning $\Delta\omega_0$ and initial phase difference $\phi(0)$ between the free running slave and the master laser. Further analysis shows that for special $\phi(0)$, the initial detuning plays indeed a role (via the locking range). But in general (see below) the parameter limiting t_{lock} is really the initial phase difference between free running slave oscillator and master laser.

Parameter	Value
ω_{free}	$4.748\,10^3$ THz
ω_{inj}	$4.745\,10^3$ THz
I_{free}	70 mW
I_{inj}	50 µW
Q	30

$\Rightarrow \omega_{\text{R}} = 4.23\,\text{THz}$

Table 2.3.1: Example parameters for the free running diode and the injected signal. The quality factor of the laser diode oscillator was estimated to be $Q \lesssim 30$, from the range of ω_{free} for which injection was achieved.

The center slave frequency, thus $\Delta\omega_0 = \omega_0 - \omega_{\text{free}}$, can easily be tuned via the operating temperature of the diode. In the following, the values from Table 2.3.1 are used for the involved parameters. These values are considered realistic for our experimental setup and are not normalized, to get a feeling for orders of magnitude. The locking range ω_{R} and the quality factor Q are only estimated, and Section 4.2 explains how their respective values were found. For simplicity, a specific slave frequency was chosen, although the output of the free running laser diode is typically not single mode.

Figure 2.3.3 a) shows the simulated transient frequency lock for various slave frequencies around ω_{free}. The initial phase difference $\Delta\phi = \phi(0) - \phi_\infty$ was kept constant at $\Delta\phi = \phi_\infty = \arcsin((\omega_{\text{free}} - \omega_{\text{inj}})/\omega_{\text{R}})$. As ω_{free} is tuned through the locking range, ϕ_∞ undergoes a phase shift by π, so the total amount of phase the slave has to catch up until it locks varies significantly. From Table 2.3.1 it can be seen that ω_{inj} was chosen smaller than ω_{free}, which explains why negative initial detunings $\Delta\omega_0$ lock faster than positive.

In Figure 2.3.3 b) the initial detuning $\Delta\omega_0$ is kept fixed, and $\phi(0)$ is varied (effectively the initial phase lag $\Delta\phi$). For values close to ϕ_∞, the locking is exponential, and for $\phi(0) = \phi_\infty$ we even get instantaneous locking[2]. It is easily seen, which $\phi(0)$ lies close to the unstable stationary phase $\phi_\infty^{\text{unstable}}$ (see eq. (2.3.6) and Figure 2.3.2). The locking behavior for these initial values is very different to the ones close to the stable point. At first $\omega(t)$ even diverges from ω_{inj} before coming back and settling. Figure 2.3.2 explains this peculiar behavior. For $\phi(0) > \phi_\infty^{\text{unstable}}$ the time derivative of $\phi(t)$ is positive and runs off to the stable solution $2\pi + \phi_\infty$ (as indicated by arrows). The instantaneous frequency given by (2.3.2) is defined for phase values $\phi \in [-\pi, \pi]$, so as soon as ϕ leaves this interval on one side, coming back on the other side with a flipped sign, the change in frequency gets reversed. The important consequence is that the locking time is increased, as the slave catches up a larger phase difference before settling.

After this detailed discussion of transient injection locking, a real-world injected laser diode can be analyzed.

[2]This locking is really instantaneous! The physical reason is that the oscillator circuit has phase "memory" but lacks it for the frequency. The frequency can thus be changed instantaneously, whereas the phase changes smoothly (see [3, 9]).

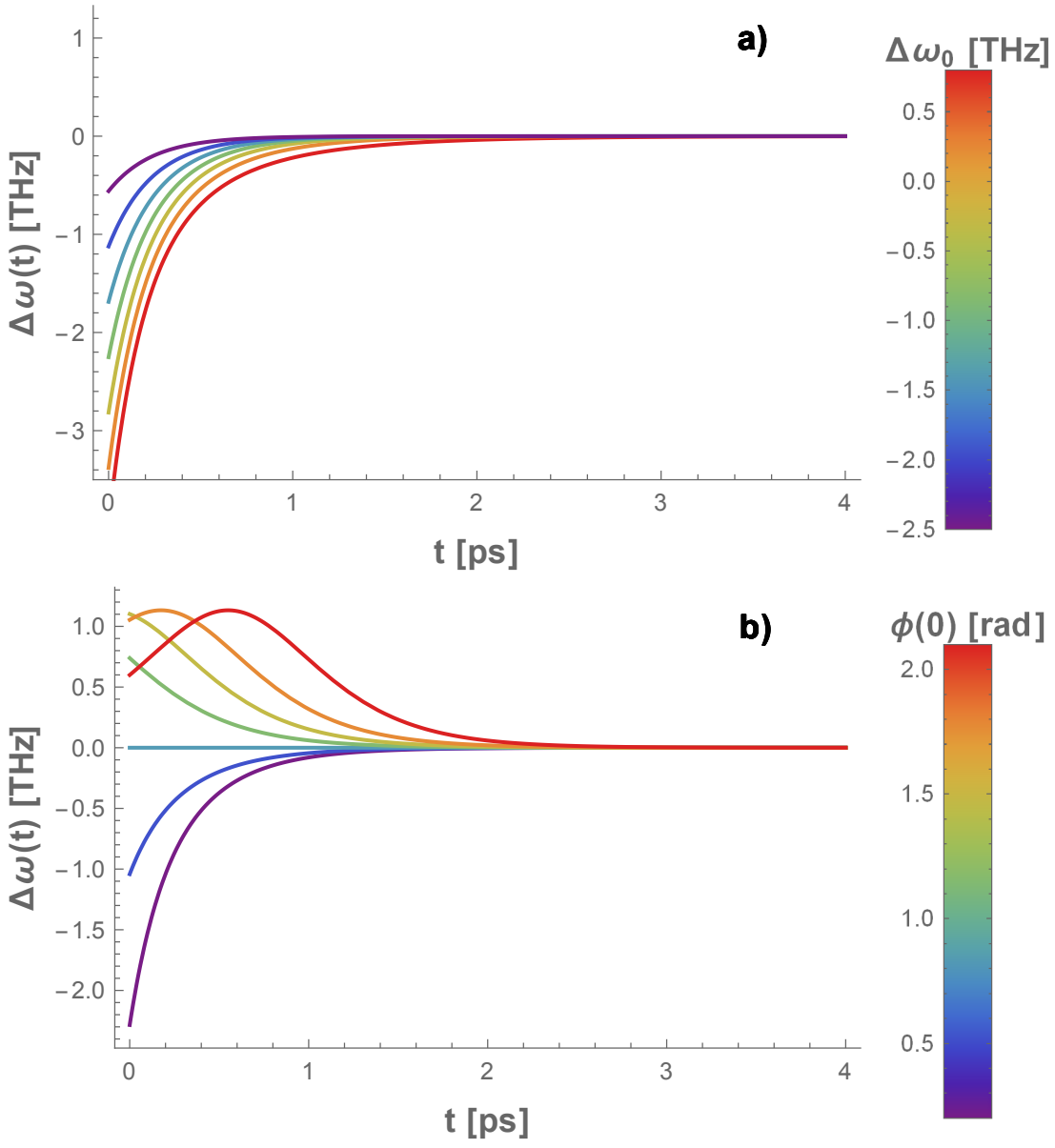

Figure 2.3.3: Simulated frequency response of the slave for a suddenly turned on master signal. The y-axis shows $\Delta\omega(t) = \omega_{\text{inj}} - \omega_{\text{osc}}(t)$. In a) the initial phase difference is always ϕ_∞. In b) the initial slave frequency is fixed at ω_{free} and the phase is varied. All other parameters are kept fixed, at values given in Table 2.3.1. Note the instantaneous frequency jump in every case from $\omega_0 - \omega_{\text{free}} \to \Delta\omega(0)$. In b), for $\phi(0) = \phi_\infty$ frequency locking happens instantaneously.

Chapter 3

Characterization of the Optical Injection Setup

The following chapter describes how a blue semiconductor laser diode[1] was injection locked to a 396.96 nm master laser. Optical output power vs. current of the laser diode is found in Appendix B. It is sometimes possible, that a laser diode is only partially locked to the injected light. The quality of the injection was therefore checked in two different ways and we came to the conclusion that almost full injection locking was realized. The complete sketch of the setup (including experiments from Chapter 4) can be found in Appendix C. For clarity, only small block diagram sketches are used in the following, as the detailed description of the setup is not of much interest for the discussion.

3.1 Setting up an Optical Spectrum Analyzer

To check if the laser diode was injected, an optical spectrum analyzer (OSA) was built in the form of a half-confocal Fabry-Perot cavity (see [15] for the advantages of such a configuration). After finding a compromise between free spectral range (FSR) and linewidth (see Table 3.1.1 for the final values) the spacing between the mirrors was fixed by a 74.3 mm Invar©-tube[2], which had a piezo stack glued onto one side. The flat mirror was glued onto this piezo stack, and the curved mirror directly onto the tube. The Invar©-tube inhibited relative motion of the mirrors, thus stabilized the transmission frequency. By placing the OSA on a custom-made holder underlaid with neoprene I was able to reduce vibrations of the cavity and could stabilize the transmission intensity. A linewidth around 20 MHz could be achieved by incoupling the master light, which was known to have a linewidth of 500 KHz. The linewidth was expected to be around 3.3 MHz, based on the specified reflectivities of 0.996 and 0.993 of both mirrors. The transmission line broadening was probably due to intra cavity absorption by dust (leading to estimated round trip losses of at least 3%). This OSA was not supposed to be a high-finesse cavity so the broadened linewidth was not investigated further. It served well as a tool signaling injection.

[1] Nichia NDU4316E
[2] American Elements

Parameter	length	FSR	linewidth	$P_{\text{out}}/P_{\text{in}}$
Value	80.3 mm	1.8 GHz	20 MHz	0.01

Table 3.1.1: Parameters of the custom built optical spectrum analyzer.

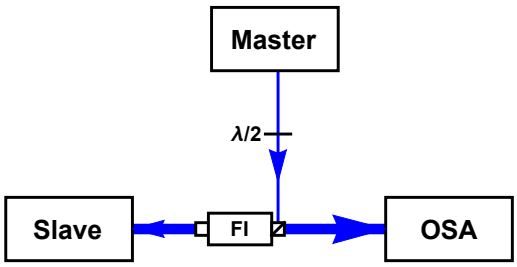

Figure 3.2.1: Sketch of the basic laser injection locking setup. The Faraday isolator (FI) protects the slave from optical feedback. The waveplate matches the master polarization with the isolator side port polarizing beam splitter.

3.2 Points of Clean Injection

Optical injection locking of a semiconductor laser diode is not only sensitive to the injected power, but also to the temperature of the diode and the current applied to it[3]. This is easily understood, by remembering that an important part of a laser is its lossy cavity. Changing the applied current or the temperature will obviously change the supported cavity modes. Any injected light will only be resonant if the operating conditions allow it to excite a mode in the cavity. If these conditions are not met within a range determined by the gain function, the cavity finesse and the injected power (see Section 2.1), additional modes (possibly not injected, but originating from the free running diode) will be excited, and one no longer talks about a *clean injection* [6, 7].

The basic setup for optical injection locking is presented in Figure 3.2.1. The injected light leaving the slave diode was incoupled into the OSA, such that only the ground modes (TEM_{00}) were transmitted (see Figure 3.2.2). Unlike the slave diode the master laser was single-mode, therefore the points of clean injection were easily found by optimizing the current applied to the diode until the OSA signal was also single mode.

A systematic high precision temperature-current scan over all clean injection points was not performed, due to expected drifts in the diode temperature (see [6]). Points of clean injection spaced by $10 - 13$ mA and $1 - 2$ mA wide were found for all temperatures between 15 and 25 °C and operating currents between lasing threshold (33 mA) and damage threshold (145 mA) agreeing with [7]. This was expected, since for this range of parameters the largest achievable difference between slave and master wavelength was only around 0.7 nm (see Section 4.2) and the master frequency was inside the locking range around the slave.

[3] Controlled by Thorlabs LDC 200C and Thorlabs TED 200C respectively

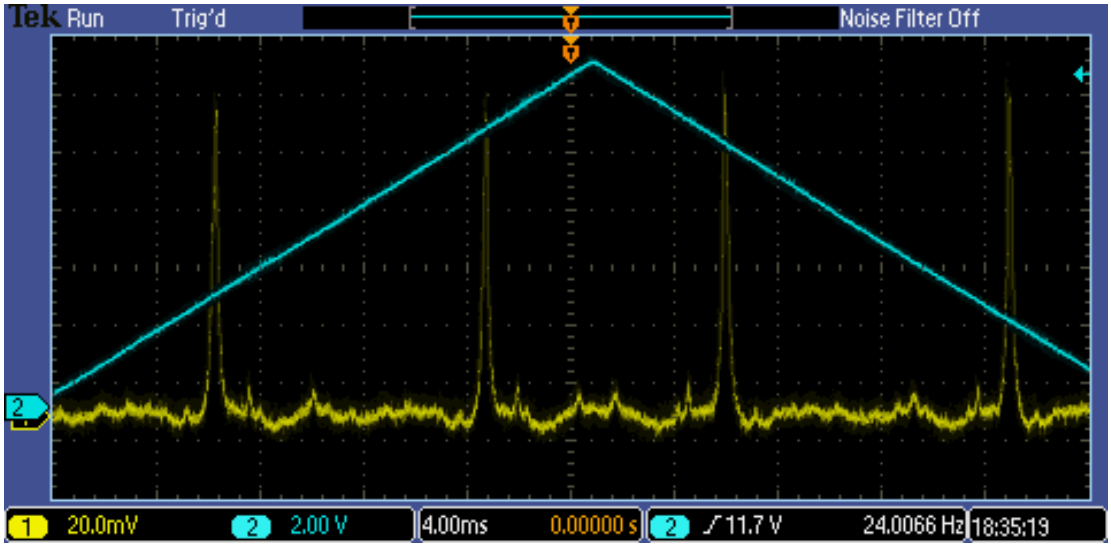

Figure 3.2.2: Typical clean injection signal on the oscilloscope when scanning the length of the OSA. The blue triangular line shows the piezo voltage ramp, the yellow line shows transmission peaks of the injection locked light.

3.3 Spectral Purity of the Injected Light

As mentioned before, the transmission linewidth of the OSA was higher than that of the injected master light, so as a precautionary measure the frequency of the slave output was compared to the frequency of the master light in a beat note experiment (see Figure 3.3.1).

Before hitting the slave laser diode, the master laser was sent through an acousto optic modulator[4] (AOM) in a double pass setup. The AOM was operated at 80 MHz, thus shifting the master frequency by 160 MHz. A small portion of the master light was picked off before hitting the AOM and sent on one input port of a beam splitter. The injected slave light was sent onto the second input port of the beam splitter thereby superposed with the original master light. The polarization of master and slave light was matched using a $\lambda/2$ waveplate. At this point, the interfering light ideally consisted of only the master light and the slave light, injected by the 160 MHz shifted master light. Both signals created an amplitude modulated (AM) intensity signal, which was detected with a fast photodiode[5] (fast PD). The beat note was observed on a spectrum analyzer at 160 MHz as expected (see Figure 3.3.2). A Lorentzian fit yields a full width at half maximum (FWHM) of 30 Hz, limited by the resolution of the spectrum analyzer. Clean injection points were visible from 50-145 mA at 25°C (thus optical powers of 4-130 mW at 396.96 nm). Frequency stabilized light was successfully created for powers up to 130 mW and will be of use in our laboratory.

Besides from checking the frequency stability of the slave light, the beat note experiment had two other uses. One appealing feature was the easy and precise determination of points

[4] IntraAction Corp. ASD-802B8.397
[5] Thorlabs PDA10A-EC

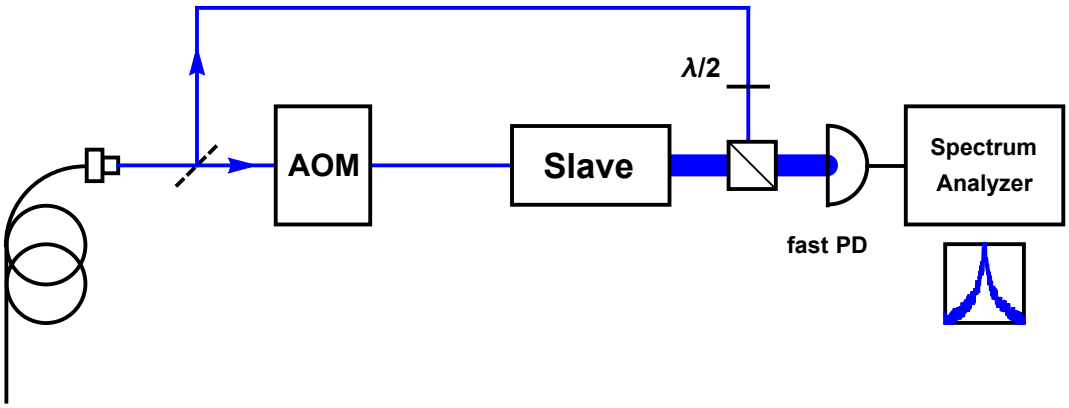

Figure 3.3.1: Sketch of the beat note experiment. The spectrum analyzer decomposed the AM signal from the fast PD into its frequency components (sketched in blue).

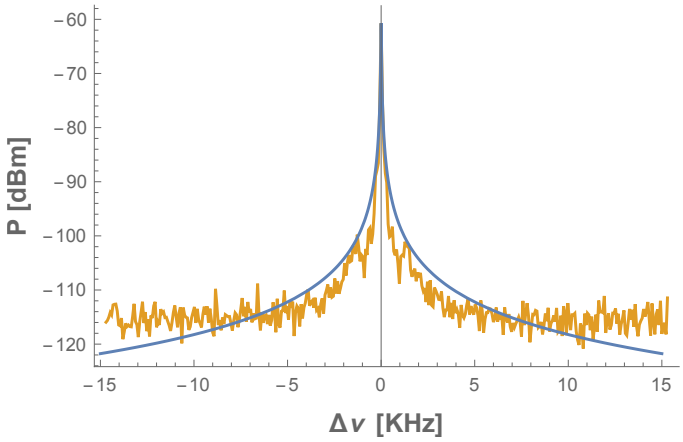

Figure 3.3.2: Beat note of the master and the 160 MHz shifted injection locked slave. The solid line is a Lorentzian fit of FWHM 30 Hz, limited by the resolution of the spectrum analyzer.

of clean injection (basically agreeing to the points found by optimizing the OSA signal). For a fixed temperature, the correct current resulted in minimal width and maximal peak height of the beat note. A clean injection using a frequencystabilized master should have a sharp peak, as the phases noise from the slave gets suppressed maximally for frequencies around the master frequency (for detailed explanation see [10], for a beautiful spectrum see [16]). The second application was to apply AM on the master light and determine how the slave output would depend on these additional frequency components. This follow-up project will be discussed in the next chapter.

Chapter 4

Filtering and Switching Behavior of an Injected Laser Diode

4.1 The Laser Diode as a Frequency Filter

Active frequency control of a laser using a feed back loop often trades noise between two frequency regions. This general behavior of shifting noise in one region to another, can essentially be characterized by a conservation law [17]. One example in the TIQI lab is the locked 729 nm laser addressing the qubit transition. Its linewidth is narrowed down at the expense of creating frequency noise (called "servo-bumps" in the following, see [6]) at a spacing of roughly 1 MHz to its center frequency . If we were only interested in the central frequency, called the carrier, this would not influence the experiments. In our case however the ions in the trap can not only be excited at their carrier qubit transition-frequency, but also at frequencies $\omega_0 \pm \omega_{\text{trap}}$ called blue and red sideband transitions. These sidebands originate from the trapping fields being operated at the trap frequency ω_{trap}, in our case $\omega_{\text{trap}} \approx 1$ MHz. The experiments are thus affected by servo-bumps coinciding with the sidebands. Hence, every time one of the sideband transitions is driven, the carrier transition is excited as well which can lead to unwanted qubit flips, thus reducing the fidelity of quantum operations (see Section 7.2). The idea was now, to check if an injected diode could filter out frequency components in the master light, maybe filter out even the servo-bump frequencies. The reasoning behind this, is that the spectral gain profile of the injected laser diode is shifted and narrowed down. As can be seen in Figure 4.1.1 modes where the gain is below threshold might then not be amplified enough to lase, thus being completely suppressed. These frequencies were introduced by sending the master light through an AOM and amplitude modulating the RF drive of the AOM with frequencies in a region $\omega_{\text{MOD}}/2\pi = 400 - 3000$ KHz.

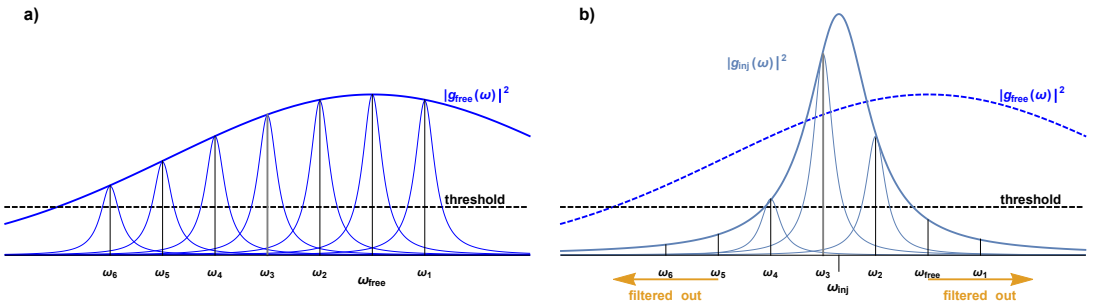

Figure 4.1.1: **a**) Schematic gain spectrum for the free running slave. **b**) Schematic gain spectrum for the injected slave. The strongest mode is taken to be the center frequency of the injected slave light. The lasing modes are show as Lorentzians (seven in **a**) and only three in **b**)).

4.1.1 Calibration

Using the same AOM double pass setup as in Section 3.3, the beat frequency at 160 MHz was modulated. A mixer[1], combined the signal from an RF source[2] with a sine output by a wave form generator[3] (WFG) . Changing the offset of the WFG signal, tuned the modulation index

$$A_{\mathrm{MOD}} = \frac{1^{\mathrm{st}}\ \text{sideband power amplitude}}{\text{carrier power amplitude}} \cdot 100 \tag{4.1.1}$$

of the RF drive between 20 and 80%.

As the diffraction efficiency of the AOM varies for different drive frequencies, calibration of the modulation index B_{MOD} produced by the AOM in the master light was required. For this, the unmodulated master light was beated against the master light after the AOM. Figure 4.1.2 a) shows the optical power recorded by the fast PD. The carrier beat note at 160 MHz, as well as the red and blue sidebands spaced from the carrier by $\pm\omega_{\mathrm{MOD}}/2\pi = \pm 400$ KHz are visible, together with higher order sidebands. These higher order sidebands on the fast PD are due to the AM RF signal driving the AOM, which already contains them. The AM master spectrum was then recorded for different ω_{MOD} and the relative amplitude of the carrier and the first sideband was measured. The results are shown in Figure 4.1.2 b). Figure 4.1.2 c) depicts the dependence of the AM signal driving the AOM on ω_{MOD}. As we can see, the mixer behaves very linearly over the whole modulation frequency range. The modulation index B_{MOD} of the master light is 35% lower than A_{MOD} and decreases faster as is depicted in Figure 4.1.2 d) (for $A_{\mathrm{MOD}} = 25$ % the data was very noisy). This indicates that the AOM slightly suppresses out higher ω_{MOD}. The effect was taken into account when analyzing the slave light.

4.1.2 Modulated Injection

The AM master light passing through the AOM was used to inject the laser diode. Figure 4.1.3 shows the basic working principle of the experiment. Furthermore, one can schematically see

[1] Mini-Circuits ZLW-3+
[2] HP 8640B-Signal Generator
[3] Gw Instek SG-1013

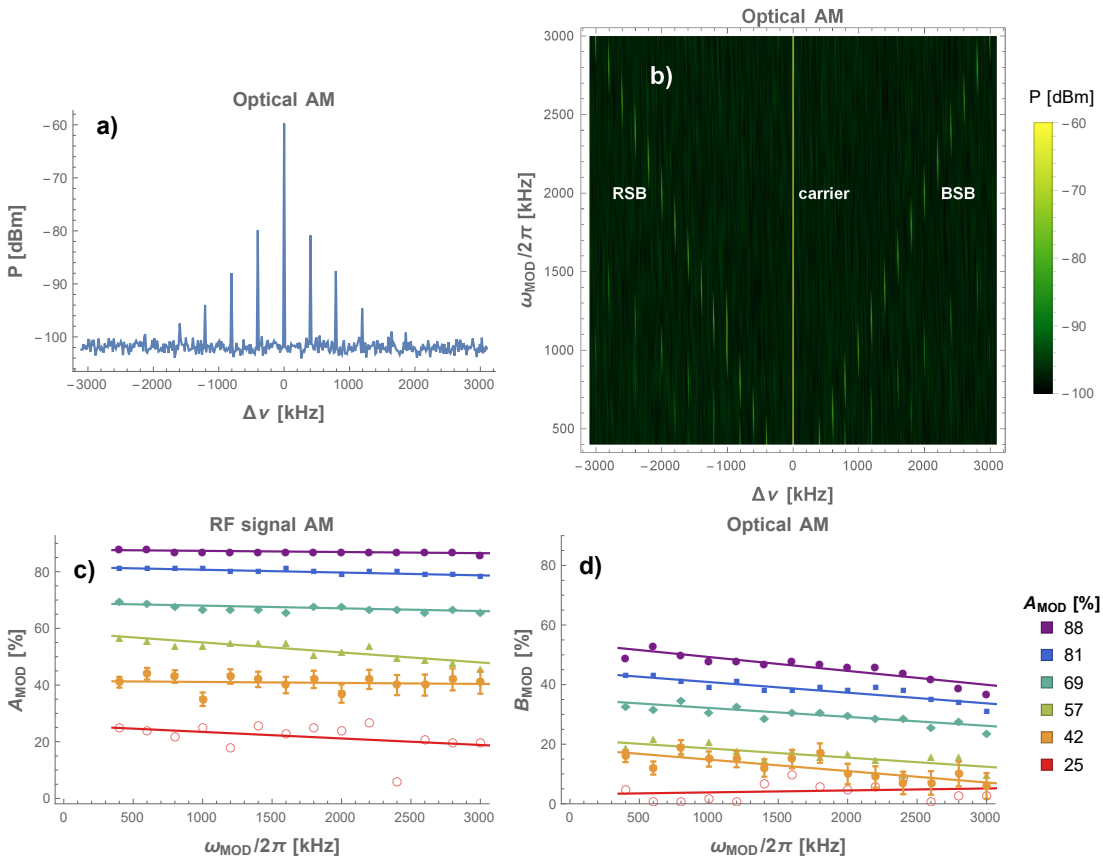

Figure 4.1.2: **a**) Spectrum of the AM master light around $\omega_{\text{inj}}/2\pi$. **b**) 2D scan of spectra like a) for different ω_{MOD} in steps of 200 KHz. BSB and RSB denote the blue and red sideband at $(\omega_{\text{inj}} \pm \omega_{\text{MOD}})/2\pi$ respectively. Both 2^{nd} and 3^{rd} sidebands are also visible. **c**) Deduced values of A_{MOD} from taking the maximum value of carrier and first sidebands for the spectra like the one shown in **a**), as a function of ω_{MOD} for varying modulation strength. **d**) Modulation index B_{MOD} of the master light after the AOM as a function of ω_{MOD} for different A_{MOD}. Also shown are linear fits (the lowest point in **c**) is an outlier and was not taken into account for fitting). Note the steeper slope of B_{MOD} compared to A_{MOD}, indicating that RF signal AM is attenuated when converting it to optical AM with an AOM. For clarity, error bars are only shown for $A_{\text{MOD}} = 42$ %. They increase with ω_{MOD} and decreasing A_{MOD}.

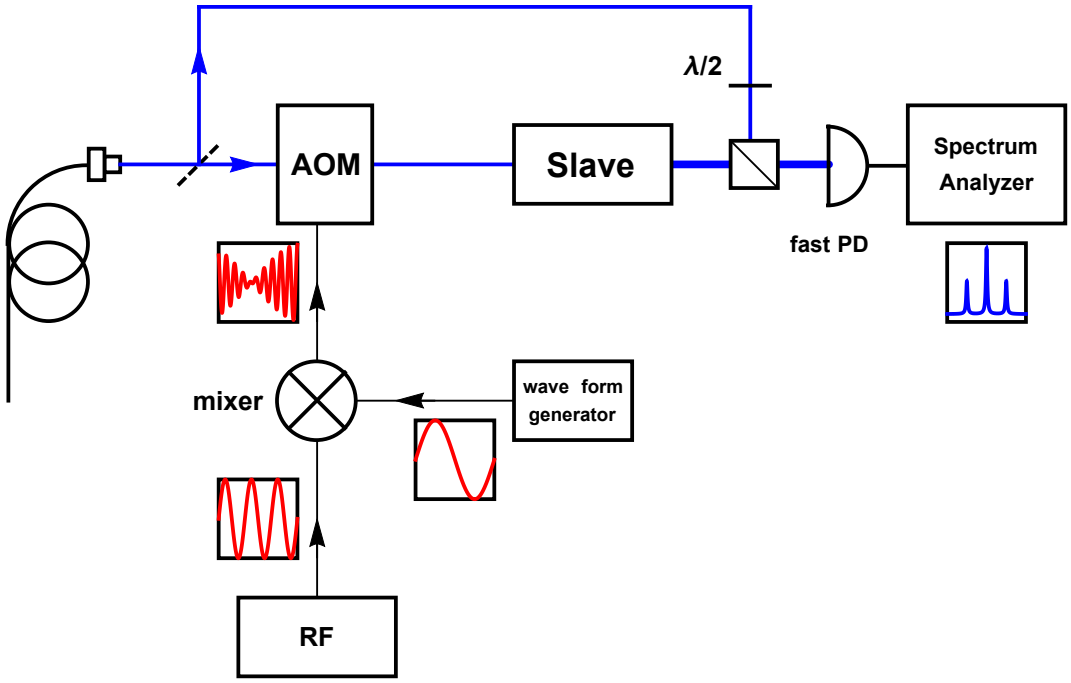

Figure 4.1.3: Sketch of the modulation experiment. Signals from the RF source and the wave form generator applied to the mixer, and the resulting AM signal fed to the AOM are sketched in red. The spectrum analyzer decomposes the AM signal from the fast PD to its frequency components sketched in blue.

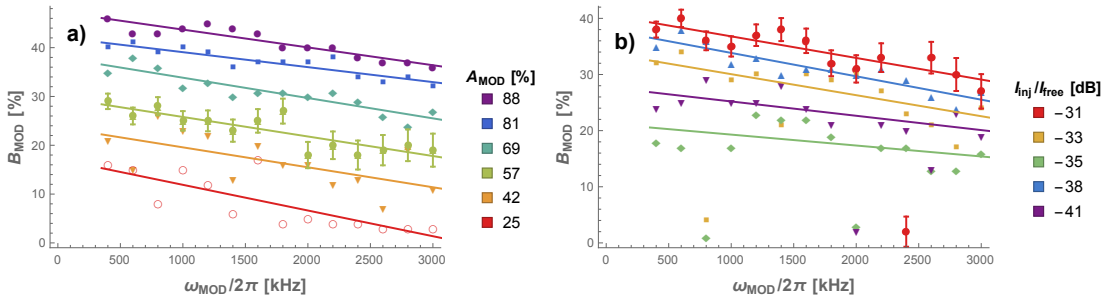

Figure 4.1.4: a) Dependence of slave modulation index B_{MOD} on AM frequency ω_{MOD} for various modulation indices A_{MOD} of the AM RF signal. b) Same as a) but for various ratios of master and slave intensities.

the modulated RF signal applied to the AOM (red), as well as the signal obtained from the spectrum analyzer (blue). The outcoupled light from the slave diode was beated against the original, unmodulated master light. The AM frequency was varied from 400-3000 KHz, the fraction $I_{\mathrm{inj}}/I_{\mathrm{free}}$ of the carrier frequencies from -41 to -31 dB and the modulation index A_{MOD} of the electric AM RF signal driving the AOM between 25 and 88 %. Surprisingly, B_{MOD} of the master light was not altered significantly by the slave diode. Figures 4.1.4 a) and b) show the dependence of the modulation index B_{MOD} of the slave light on ω_{MOD} for varying A_{MOD} and I_{inj} respectively. Reference [2] discusses how the master AM translates to the slave AM in an infrared laser diode. Its main result for our purposes is shown in Appendix D. According to it, low ratios of $I_{\mathrm{inj}}/I_{\mathrm{free}}$ can lead to -130 dB master AM suppression by the slave. For our parameter range, suppressions as high as 60 dB corresponding to a factor of 10^6 should be possible. Comparing to Figure 4.1.2, we only see a suppression of several percent.

There is however a region of modulation frequencies, where the master AM is amplified. The calculations presented in [2] were not performed, but the absence of suppression in our experiment might suggest that modulation frequencies were probed, for which the suppression is extremely low. The error bars in our data indicate that the data is not very good, but still, significant filtering (noise reduction of for example an order of magnitude) should have been detected. At the present point of investigation, it can at least be stated, that frequency-noise filtering by optical injection of a blue laser diode is not easily achieved. Filtering might happen at much higher modulation frequencies, where the AM response of the AOM becomes significant.

If the slave does not filter out any frequency components at 397 nm, then AM master light could be amplified by optical injection locking. Quantum operations like the Mølmer-Sørensen gate would directly benefit, as powerful AM light could be easily produced. The abscence of AM suppression could prove extremely useful in creating a whole range of sidebands around a carrier frequency with just one AOM. Considering the size and price of these devices, this could help scaling up ion trap experiments.

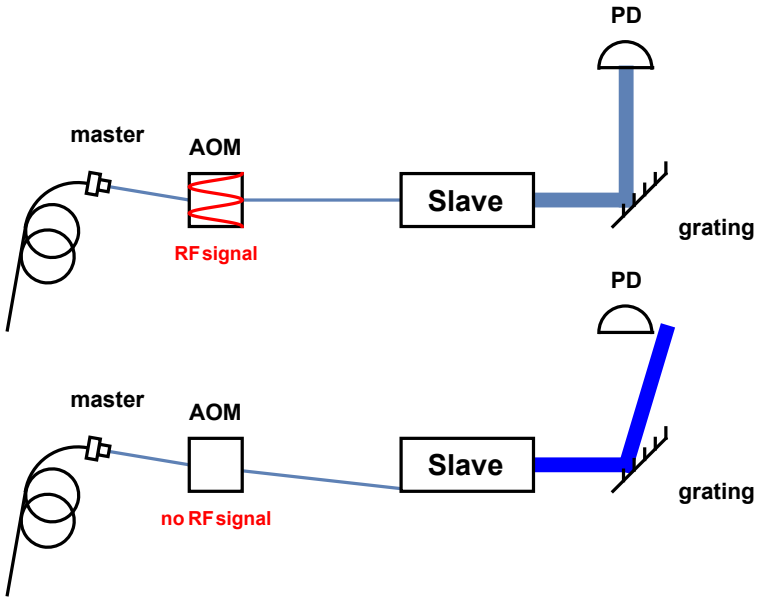

Figure 4.2.1: Spatial separation of injected and non-injected laser diode light.

4.2 Switching the Injection On and Off

4.2.1 The Setup

As was established in Section 2.3, injecting the slave diode with ω_{inj} inside the locking range forces the slave output frequency to jump from ω_{free} to the master frequency ω_{inj}. If ω_{free} does not coincide with ω_{inj}, turning on the injection will change the output frequency of the slave (see Section 2.3.2). The easiest way to discriminate between those two frequencies, is to spatially separate ω_{free} and ω_{inj} with a dispersive element such as a diffraction grating (see [7]). The basic working principle is shown in Figure 4.2.1. To calibrate the free running slave wavelength, a screen was placed roughly 6 m after the grating[4] and the spatial separation between the free running laser spot and the injection locked spot (at 396.98 nm) recorded for different diode operation temperatures. The temperature of the diode was varied between 15 and 25 °C. The maximum temperature was specified by the manufacturer to be 30°C, and going below 15°C introduces the risk of condensation water in the diode. At 15 °C the separation of the free running diode spot to the injected spot was 5 mm, opposed to 2 mm at 25 °C. Knowing that the grating has 1.25 mrad/nm dispersion, the laser diode frequency was estimated to lie in a range between 396.3 and 396.7 nm. The higher wavelength at 25°C was chosen because the quality of the injection was better (since the master frequency was deeper inside the locking range). The optical power output was not sensitive to temperature (see Appendix B) as it varied by less than 1% over the whole temperature range when keeping the current fixed.

After determining the free running laser wavelength, the injection could be switched in four

[4] Thorlabs GR25-1205

different ways:

- tuning the current of the slave to allow injection or not
- tuning the temperature of the slave to allow injection or not
- blocking the master with an optical chopper
- switching the AOM on and off, thus illuminating the laser diode with the master laser or not.

Since we lacked control and speed over the the first two mechanism, we opted for the chopper and later the AOM as switching tools.

4.2.2 Slow Switching

The chopper[5] switched the master light fairly slowly compared to the AOM, which resulted in very different rise times of the master and the slave signal. Both signals are shown in Figure 4.2.2 a). The different rise times result from the Gaussian nature of the master laser beam. Equation (2.1.5) shows that for a fixed detuning $\omega_{\text{free}} - \omega_{\text{inj}}$ and a slave output intensity I_{free} that locking the slave requires a certain master intensity I_{inj}. As the chopper blade sweeps over the master beam, more and more power is delivered to the slave, until the locking condition is satisfied (see Figure 4.2.2 b)). For the present settings (see Table 2.3.1) and a master beam with 1 mm spot size, $I_{\text{inj}} \approx 40$ µW is estimated. Fitting an error function to the data and differentiating it, roughly reproduced the expected master Gaussian beam. The intensity hitting the slave at the onset of the slave signal was estimated around 70 % of its total value, in other words 36 µW. Higher chopper frequencies simply resulted in the chopper sweeping faster over the master laser beam, thus reducing the master rise time as can be seen in Figure 4.2.2 c). The faster the chopper sweeps over the master beam, the faster the slave is provided with the threshold master power, so it becomes sooner clean injected. The quicker the slave gets clean injected, the shorter its rise time will be on the PD (partial injection happens for master power below clean injection threshold and leads to a small signal on the PD). From Section 2.3 one would expect rise times in the pico second range, so the master rise time clearly limits the slave rise time. The non-linear behavior dependence of rise time to chopping frequency is due to the circular geometry of the chopper. The rise times were measured using the 10-90 % criterion of the fitted error functions.

4.2.3 Fast Switching

The AOM could switch the master laser much faster then the chopper. Its driving signal was turned on and off with an RF switch[6], controlled by a wave form generator producing TTL step signals (1 ns rise time). The setup is sketched in Figure 4.2.3 with the different RF signals indicated in red, and the observed PD signals in blue. The master laser was deflected periodically and its switching behavior was monitored by a fast PD. The master signal had a rise time of approximately 50 ns. This can be explained as follows: once the AOM is turned on, the acoustic RF wave in the AOM-crystal has to travel several mm to and through the laser beam. The

[5] Thorlabs MC2000-EC
[6] Mini-Circuits ZASW-2-50DR+

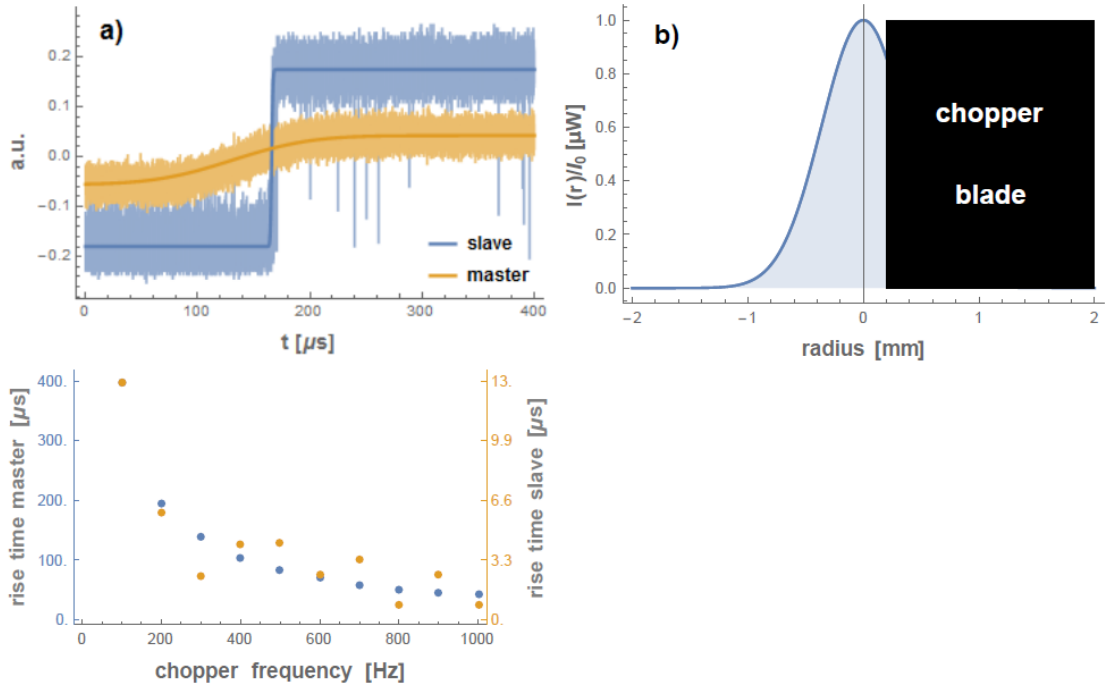

Figure 4.2.2: a) Trace of the chopped master signal and the slave following the master but with a much shorter rise time. The solid lines are error-function fits to the data. b) 70 % of the master Gaussian beam intensity is needed for injecting the slave. The rest is blocked by the chopper blade. c) Behavior of the master and slave rise time for varying chopping frequency.

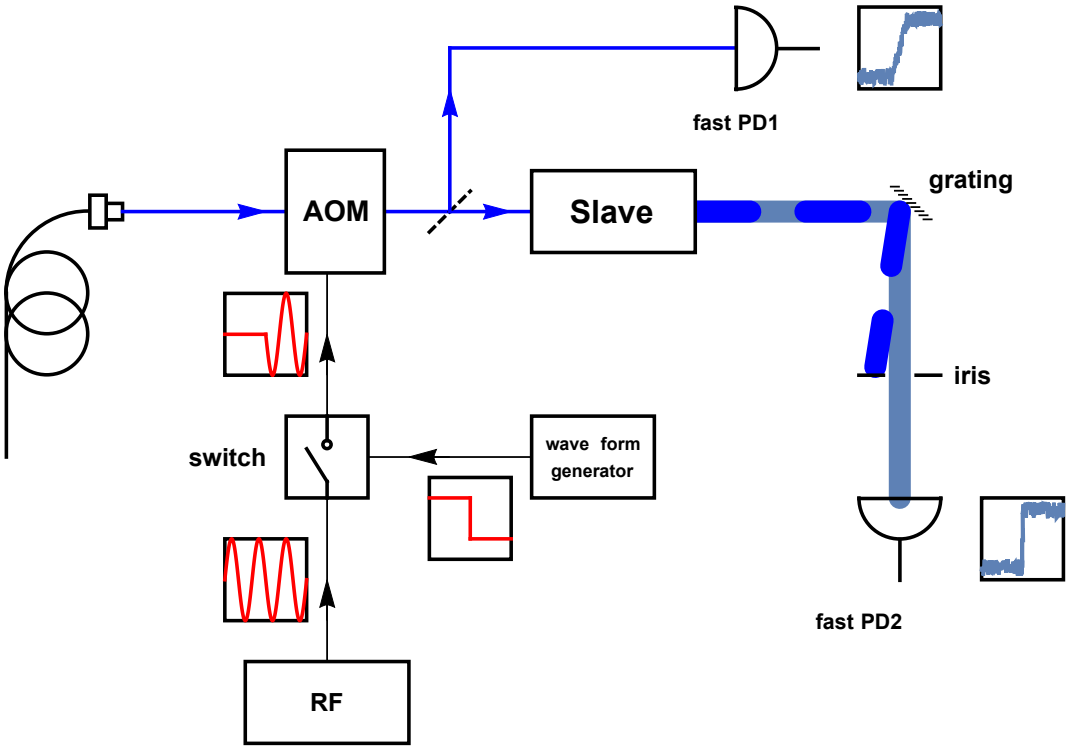

Figure 4.2.3: Schema of the switching setup.

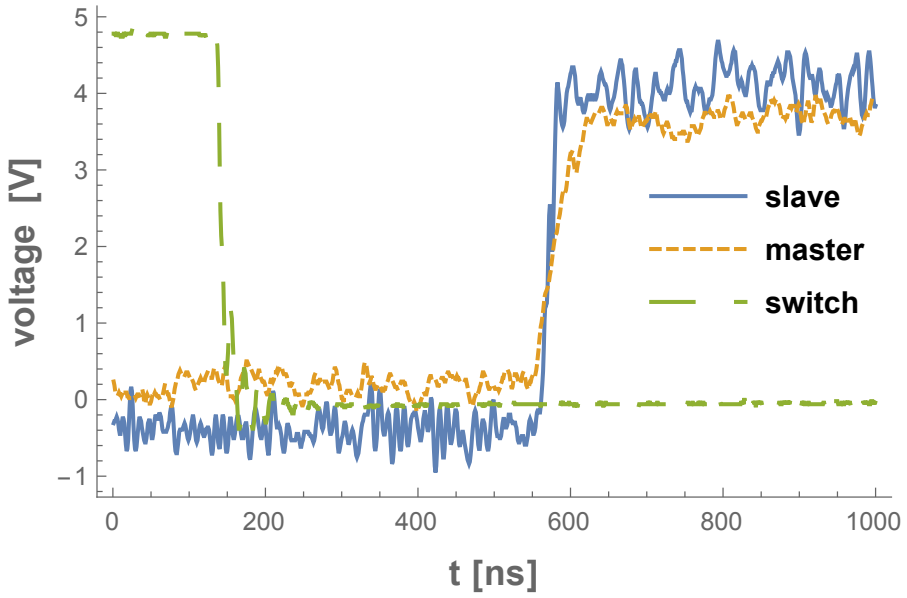

Figure 4.2.4: All signals involved in the switching experiment on the oscilloscope. The dashed line shows the TTL signal to the RF-switch, the dotted and solid lines show the optical signals from master and slave light on PD1 and PD2, respectively. For clarity, they are shifted by +2.5 V and multiplied by a factor 300 and 5 respectively.

speed of sound in the crystal is 5.56 mm/µs so the portion of the master beam deflected into the first order rises in a finite amount of time. It will illuminate the PD at its full intensity only after the RF wave has crossed the whole laser beam in the AOM.

The master laser only hit the slave when the AOM was turned on (as indicated in Figure 4.2.1), so the beam was deflected periodically by the grating. An iris blocked the non-injected light (see Figure 4.2.3), such that only the injected slave light hit PD 2. Residual non-injected light of the slave caused a noise floor on the PD. After the grating, the total beam path was around 2 m, in order to reach good extinction of non-injected light.

Figure 4.2.4 shows all three signals involved in the switching experiment: the electric TTL signal, the switched master laser on PD 1 and the slave light on PD 2. The qualitative behavior of the signals is the same as in the chopper experiment. Traces were recorded for different slave output powers and the signals fit with error functions. The result is shown in Figure 4.2.5. Slave signal rise times around 20 ns are observed, being less than half the master signal rise time. This agrees well with the slow switching experiment discussed in the previous section, where we established that the slave needs more than half of the master beam to be locked. As a rule of thumb, we can state that the slave is locked to the master after at most 50 ns.

The turn on of the injection is limited by the speed of sound in the AOM crystal. From the theory developed in [9] and presented in Section 2.3, it was already expected that the AOM limits the locking time, as it can be estimated at roughly

$$t_{\text{lock}} \approx 4 \cdot \frac{1}{\omega_{\text{R}}} \approx 1\,\text{ps}$$

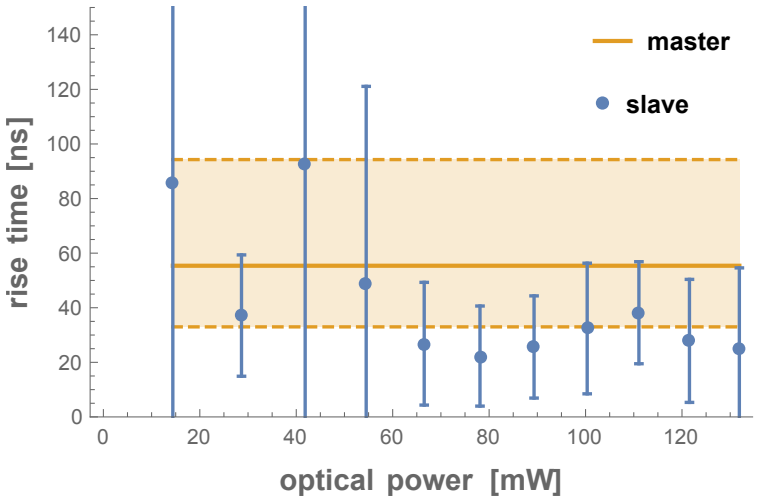

Figure 4.2.5: Rise times of the optical signal of the slave diode for different output powers. The shaded area is the uncertainty of the rise time of the master laser.

which is much faster than even the rise time of the TTL square pulse (≈ 1 ns). If the locking time was not limited by the master, the locking time should increase for higher slave output powers as the locking range would decrease. No such trend is observable. Experiment and theory thus agree very well. Comparing with e.g. [9] one clearly sees the effect of the extremely high locking ranges at optical frequencies. Consequentially, if we would consider injection locking in electrical LC-circuits, more care would be required, since rise times on the order of tens of nanoseconds are expected due to the much narrower locking range. Section 2.3.2 also discussed, that the initial phase difference between the injected light and the free running laser diode can have a large effect on the locking time. Namely, if

$$\phi(0) = \pi - \phi_\infty = \phi_\infty^{\text{unstable}}$$

we would get the longest rise time. If the relative diode and the master light phase could be controlled, long slave rise times not limited by the master turn-on might actually be observed directly. Shortening the rise time of the master light might be possible by focusing the beam tightly as it goes through the AOM, but a locking time on the order of pico seconds is out of reach for now.

The theoretical framework presented in this thesis has a minor flaw because the locking range ω_R depends on the quality factor Q of the laser diode cavity. This parameter can be measured, but we simply estimated it to get a feeling for the involved orders of magnitude. Recently a way to calculate the locking range without knowing anything about the quality factor of the injected oscillator has been developed [19] for LC-circuits. In essence this approach treats injection locking very generally as perturbation problem. The oscillator can be characterized by a perturbation projection vector (PPV) which describes the phase sensitivity of the state space elements of the oscillator (like the positions or electric fields). Knowing this PPV, one can average over the usually very fast phase variation of the injected signal, keeping only the much slower phase difference $\Delta\phi(t)$ between oscillator and injected signal. One ends up with a

differential equation for $\Delta\phi(t)$ of which the Adler equation is a special case. We did not apply this analysis yet, but plan to apply it to laser diodes and perform it in the future.

Chapter 5

Conclusion and Outlook

The main result of this project was the successful injection of a high power 397 nm semiconductor laser diode, which relieved partially the power shortage at this wavelength in our lab. We were able to characterize the quality of our injection with an optical spectrum analyzer built as part of this project and by recording the beat note between the master and injected slave light.

Two follow-up projects investigated possible applications of the injection-setup. First, optical filtering properties of the injected laser diode were investigated with the aim to suppress noise of the master light in a range of 3 MHz around the carrier. The initial goal was to suppress servo-bump noise in the master laser introduced by our frequency control mechanisms. We simulated these frequency components by amplitude modulating the master light. No filtering could be observed. This is in direct contradiction to previous work [2] so further investigations should be performed. This work investigated laser diodes in a different parameter regime than ours. The slave wavenlength was 1550 nm and the master had no detuning. The difference in suppression might be related to the low quality factor of our laser diode cavity (as the photon reservoir of the slave is small, the AM in the master might dominate). The quality of our data can be improved and further measurements are necessary to confirm the discrepancy. Additionally, simulations of the frequency response of the slave diode should be performed based on [2]. The absence of filtering might still be beneficial, in that several frequency components in the master light might be amplified by optical injection locking, thus reducing the number of AOM's required for the creation of multiple frequency sidebands. Some quantum operations like the Mølmer-Sørensen gate could greatly benefit from amplified modulated seed light.

In the second follow-up project, we spatially separated injected from non-injected slave light using a ruled reflective diffraction grating. Theory and experiment agreed very well, as the settling time of the slave diode frequency was found to be limited by the turn on time of the AOM switching the master laser. The setup required a relatively big path length of 2 m after the grating, so we can view it as a proof-of-principle experiment. Improvements of the experimental setup could further increase data quality and reliability. Significantly higher signal-to-noise should be obtainable by optimizing the injection incoupling into the laser diode with custom optics, and coupling the light after the grating into a fiber for better extinction (we used an iris for simplicity). Stronger dispersion from a grating with higher groove density reduces the path length needed to separate injected from non-injected light. And finally, it would be preferable to have a bigger separation in wavelength between the free running laser diode and the injecting

light. This would then impose higher injection power which should not be a problem. If we manage, to put this system in a box of e.g. 20 cm side length, this technique could contribute to the scalability of systems requiring injection locked light. As a specific example, one could think of trapped ions on a chip, illuminated by laser diodes of different wavelengths. A fiber carrying all the needed wavelengths could inject the diodes, and the injected light would hit the ions, whereas non-injected light would simply miss the ions.

Part II

Towards Optical Addressing of a Single Ion

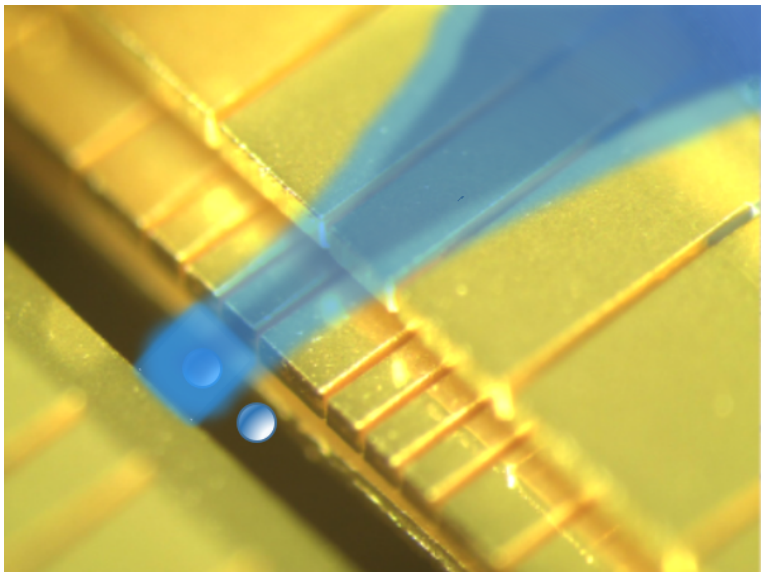

Artist's conception of single ion addressing in the TIQI segmented 3D trap.

Chapter 6

Introduction

„ ... we never experiment with just one electron or atom or (small) molecule.
In thought-experiments we sometimes assume that we do;
this invariably entails ridiculous consequences.“
— Erwin Schrödinger

In the 3D trap of the TIQI lab, ions are typically spaced around 3.5 µm. At the moment, individual ions in a chain cannot be addressed optically. Most experiments performed in the TIQI group so far use a single-ion. The main project of the second part of this master's thesis is to optically address single $^{40}Ca^{+}$ ions in our trap configuration. In other words, we built an optical system capable of focusing a 401 nm laser beam well below 2 µm spot size diameter. Single-ion addressing has been achieved in the past [21] with dedicated, highly specialized optical systems. This project was challenging because existing optics had to be upgraded in order to achieve this tight focusing. The upgrade consisted of a three lens telescope placed in front of our already installed optics.

In modeling the behavior of our optical system, Gaussian beam propagation was chosen (presented in Chapter 8). This approach was favored over ray-tracing (relying on Snell's Theorem) for two simple reasons. First of all, single trapped-ion addressing is done with a laser in its fundamental (i.e. Gaussian) mode, of which the Gaussian beam is a very good approximation. The second reason concerns the tight focusing of the laser beam. In ray optics, the focus is a single point where the intensity is not well defined. Gaussian beams allow for an estimate of the light intensity at the focus since even at this position (also called the waist location) the spot size is never zero. Knowing the intensity of the laser beam at the target ion is important because most atomic physics parameters (Rabi oscillations, transition rates, state dependent forces, ...) depend on it. It is worth noting though that ray-tracing is still a very good approximation to the Gaussian beam and served as the basis to all simulations. The outline of this part of the thesis is as follows. First we will introduce the basic notation and parameters of a Gaussian beam in order to identify the important figures of merit of such a beam, and the constraints imposed by our system. Chapter 9 describes how we came up with a system theoretically capable of focusing a 397 nm laser beam on a single-ion. We end with Chapter 10 describing the testing of the actual prototype.

Chapter 7

The Calcium Ion

In the TIQI group at ETH Zürich, $^{40}Ca^{+}$ ion experiments are performed in different traps [22, 23, 4]. As we are a group with emphasis on quantum information, we work with so called qubits (the analog of classical bits in a digital system). The next two sections, will briefly review the concept of qubit and the structure of the energy levels of the $^{40}Ca^{+}$ ion in order to discuss the transitions addressed by our lasers in the lab. The chapter ends with a short reminder of the AC-Stark shift.

7.1 Introduction to the Quantum Bit

The concept of "bits" has proven to be extremely fruitful in modern computation. A bit is just a small unit, information can be decomposed into. By doing so, an analog signal with an infinite amount of states, is converted into a digital signal composed by a string of bits. Modern computation, communication and data storage are all based on digital signal treatment and use the language of bits 0 and 1. In real-world devices, these bits can be implemented in various physical systems. The 1 could correspond to some current flowing, a voltage above threshold, light polarization or even the handedness of DNA. The 0 would then be the complementary state. If for example computers are to be miniaturized further, non-classical physics is at some point required to describe the system (as it is already the case for some parts like the transistor) and most importantly, the bits will start to behave non-classically. Quantum mechanics allows a very special phenomenon: a quantum system can be in a superposition of two configurations a the same time. So quantum mechanics allows the bit to be in a superposition of 0 and 1. In order to avoid confusion with the classical case, we write our quantum-bits as $|\downarrow\rangle$ and $|\uparrow\rangle$ instead of 0 and 1 and name them qubits. The equal superposition of 0 and 1 for example would then be written as

$$|+\rangle = \frac{1}{\sqrt{2}}|\downarrow\rangle + \frac{1}{\sqrt{2}}|\uparrow\rangle \tag{7.1.1}$$

where the factor $1/\sqrt{2}$ is linked to the probabilistic nature of quantum mechanics. This expression is an example for a wave-function describing the probability distribution of the two qubits. If the system is measured, a superposition is never seen but only one possible qubit state: $|\downarrow\rangle$ or $|\uparrow\rangle$ corresponding to the bit value: 0 or 1. Which result is recorded, is probabilistic

and defined by the square of the coefficients in the wave-function of the quantum system. Since we will measure either $|\downarrow\rangle$ or $|\uparrow\rangle$, the squares of their respective coefficients have to add up to unity. In eq. (7.1.1), we have $\frac{1}{2} + \frac{1}{2} = 1$, meaning that both outcomes are equally probable. The wave-function has many other properties, which are described in text books such as [24]. A general one qubit wave-function is written like

$$|\psi\rangle = \alpha\,|\uparrow\rangle + \beta\,|\downarrow\rangle \equiv \begin{pmatrix} \alpha \\ \beta \end{pmatrix} \tag{7.1.2}$$

with $\alpha, \beta \in \mathbb{C}$ and $|\alpha|^2 + |\beta|^2 = 1$. The second equality in eq. (7.1.2) relates the qubit superposition to a two dimensional complex vector. One can think of qubits as vectors lying on a complex unit circle, spanning an abstract state space. In this case, the basis vectors of this space are chosen as the orthogonal vectors $|\downarrow\rangle = \begin{pmatrix} 0 \\ 1 \end{pmatrix}$ and $|\uparrow\rangle = \begin{pmatrix} 1 \\ 0 \end{pmatrix}$ but, linear algebra establishes that any two linearly independent vectors can be used equally well. For example

$$|\psi\rangle = \frac{\alpha+\beta}{\sqrt{2}}\,|+\rangle + \frac{\alpha-\beta}{\sqrt{2}}\,|-\rangle = \begin{pmatrix} \alpha \\ \beta \end{pmatrix}$$

where $|\pm\rangle = \frac{1}{\sqrt{2}}\,|\downarrow\rangle \pm \frac{1}{\sqrt{2}}\,|\uparrow\rangle$, is an equally valid representation of $|\psi\rangle$. As soon as two orthogonal vectors are chosen as a basis and all wave-functions formulated with respect to them, we call these vectors the computational basis. Classical bits would restrict the state space to two orthogonal states, such as $\begin{pmatrix} 0 \\ 1 \end{pmatrix}$ and $\begin{pmatrix} 1 \\ 0 \end{pmatrix}$, whereas qubits allow a continuum of states. This is the fundamental reason why quantum algorithms can outperform classical algorithms by so much[1].

The coefficients of the wave-function $|\psi\rangle$ are related to the probability of measurement outcome $|\phi\rangle = \phi_1\,|\uparrow\rangle + \phi_2\,|\downarrow\rangle$ as

$$P(|\phi\rangle) = |\,|\phi\rangle^* \cdot |\psi\rangle\,|^2 \equiv |\,\langle\phi|\,\psi\rangle\,|^2 = |\begin{pmatrix} \phi_1^* & \phi_2^* \end{pmatrix} \cdot \begin{pmatrix} \alpha \\ \beta \end{pmatrix}|^2 = |\phi_1^*\alpha + \phi_2^*\beta|^2.$$

Intuitively speaking, one calculates the amount of $|\phi\rangle$ in $|\psi\rangle$, both expressed in the basis $\{|\downarrow\rangle, |\uparrow\rangle\}$.

The question is now, how to implement a qubit in the real world. Many ideas such as polarized photons [26], electron spins [27] or even small currents [28] have been realized. In our case, we choose the electronic energy levels of an ion.

7.2 The Quantum Bit in $^{40}Ca^+$

7.2.1 Atomic Levels for Trapped $^{40}Ca^+$ Physics

Atomic energy levels are very well suited to serve as qubits for two reasons.

1. The computational basis $\{|\downarrow\rangle, |\uparrow\rangle\}$ can be realized by very long lived atomic states.
2. Manipulation of the qubit is easily achieved by lasers.

[1] Entanglement helps in many cases, but is not the sufficient criterion for speed-up [25].

The $^{40}Ca^{+}$ ion has long-lived electron states which can be addressed at optical frequencies. Compared to microwaves, optical frequencies lead to very high electric field gradients which make the ions couple much more strongly to the applied laser fields. The availability of commercial laser sources is convenient. Further advantages of optical qubits are listed in [29]. The levels involved in our experiments are the $4^2S_{1/2}$, the two 4P levels as well as the two 3D levels (see for example [30] for the spectroscopic notation) depicted in Figure 7.2.1. These Zeeman levels are split by applying a magnetic field of 119.45 Gauss. For now, the qubit transition is the 729 nm $4S_{1/2} \rightarrow 3D_{5/2}$ transition, but future plans prefer the two qubit states $|\downarrow\rangle$ and $|\uparrow\rangle$ defined as the states $\left|S_{\frac{1}{2}}, m_J = -\frac{1}{2}\right\rangle$ and $\left|S_{\frac{1}{2}}, m_J = \frac{1}{2}\right\rangle$ respectively.

For these qubits, manipulation is achieved by a stimulated Raman transition (see [1, 29]). As this is a two photon process, it requires addressing powers of several mW, but with a decay time of $\approx 10^6$ years the $|\uparrow\rangle$ state can be considered stable [1]. The read-out of the qubit state is performed by first applying a pulse resonant to the $|\uparrow\rangle \rightarrow 3D_{5/2}$ transition, shelving any $|\uparrow\rangle$ population in the metastable $D_{5/2}$ level. The fluorescence at 397 nm is then recorded. If the qubit is in state $|\downarrow\rangle$, the transition $^2S_{1/2} \rightarrow {}^2P_{1/2}$ can be driven strongly and since the lifetime of the $^2P_{1/2}$ level is only 7.7 ns, the electron will relax and be re-excited very quickly, thus emitting many photons. Not all of these will be emitted into the solid angle the imaging system objective covers, but as soon as we see more photons than a fixed threshold value during a detection time around 200 µs, we know that the qubit was in state $|\downarrow\rangle$. On the contrary, the upper qubit state $|\uparrow\rangle$ will not scatter any photons and stay dark. Roughly one in ten times, the electron in the $^2P_{1/2}$ decays into the $^2D_{3/2}$ state, where it is no longer sensitive to 397 nm light and turns dark. It would then falsely be concluded, that the qubit was in state $|\uparrow\rangle$. In order to avoid this effect a laser called the re-pumper is needed. Its sole job is to excite the transition $^2D_{3/2} \rightarrow {}^2P_{1/2}$, thus re-pumping the lost electron into the detection cycling transition.

Using this detection scheme with a 397 nm pulse of several hundred µs, almost 100% detection efficiency can be achieved [29].

7.3 The AC-Stark Shift

As we saw in the last section, at least four lasers are need to manipulate qubit states and reliably perform read-out. All these lasers have to be resonant to their respective transition in the ion. If a laser is non-resonant to a transition, the involved energy levels get shifted. Analogously to the Stark effect induced by a static electric field, the shifting of the transition frequency by an oscillating electric field is called AC-Stark effect. An excellent treatment of interactions of quantum systems with radiation can be found in [33]. Deriving an expression for the AC-Stark shift would be beyond the scope of this work, so the well known result for far detuned radiation is simply stated as

$$\Delta E = \hbar \frac{|\Omega_R|^2}{4\Delta} \tag{7.3.1}$$

where Ω_R is the Rabi frequency of the transition of interest and Δ the detuning between radiation field and the transition angular frequency. The Rabi frequency can be calculated for a dipole-allowed transition using

$$\Omega_R = \sqrt{\frac{3\lambda^3 \Gamma P}{2\hbar c \pi^3 w_0^2}} (-1)^{J'+J+J_>-m_J} \begin{pmatrix} J' & k & J \\ m'_J & q & m_J \end{pmatrix} \tag{7.3.2}$$

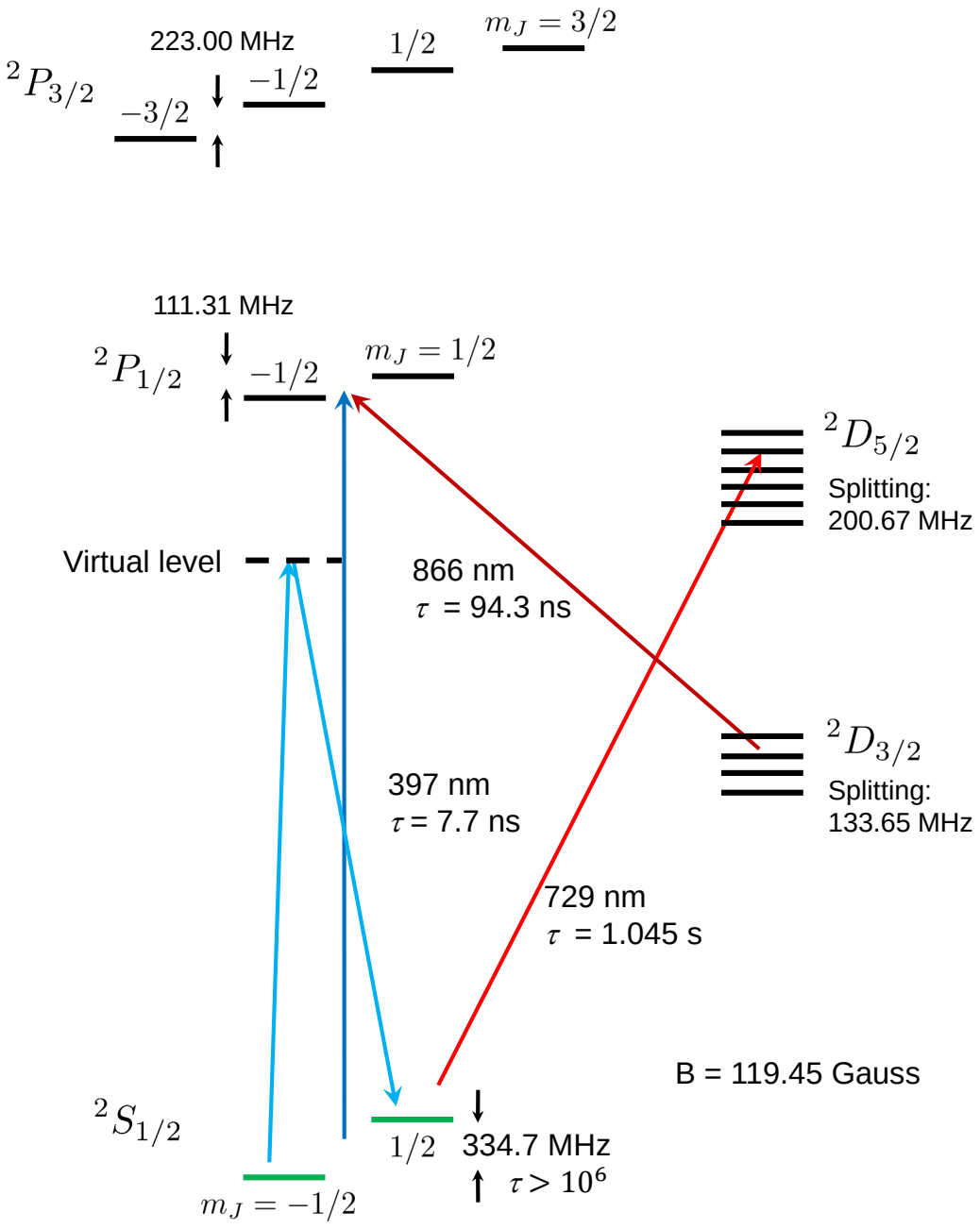

Figure 7.2.1: Basic level structure of the $^{40}Ca^+$ ion used for our ion trapping experiments. The green states are the computational basis states. The qubit Raman transition passes through a virtual level detuned far enough from the P level to avoid actually transferring the qubit to there. Note, the 3D state lying in between the 4S and 4P states.

Parameter Symbol	Explanation
λ	transition wavelength [m]
Γ	transition spontaneous decay rate [Hz]
P	laser power [W]
c	speed of light [$\frac{\mathrm{m}}{\mathrm{s}}$]
w_0	$1/e^2$ laser beam waist [m]
$\begin{pmatrix} J' & k & J \\ m'_J & q & m_J \end{pmatrix}$	Wigner 3-j symbol
J' & J	total angular momentum of lower & upper state
$J_>$	the larger of of J & J'
$m_{J'}$ & m_J	projection of J' & J
k & q	photon angular momentum & photon polarization

Table 7.3.1: Parameters needed to calculate the Rabi frequency.

derived in [34]. Table 7.3.1 explains the different parameters used in 7.3.2.

Chapter 8

Gaussian Beams

A quick review of the basic features of a Gaussian beam will provide tools to analyze and simulate optical systems. In most cases a laser beam emerges from a laser cavity. It starts from, or converges to a minimal waist location, called the focus, and diverges from this focus (perfect collimation is impossible for Gaussian beams as we will see). The intensity profile on every cross section along the propagation direction of the beam (say the $\hat{\mathbf{z}}$ axis) is a Gaussian with varying width. Wider intensity distribution leads to a bigger spot size. Tracing straight rays is a decent approximation to the Gaussian beam in the far field, but in the near field, close to the focus, the ray picture leads to erroneous results. Here, the behavior of the ion at the focus is of interest so a short introduction to Gaussian beam propagation is given. The goal of the following discussion is to give the reader an intuitive, physical understanding of the involved quantities. The detailed derivations can be found for example in [8].

8.1 Characterizing a Gaussian Beam

A laser cavity usually consists of at least two mirrors from which at least one is curved. The exiting light field $E(x, y, z)$ (more precisely the phasor amplitude of its electromagnetic field) varies rapidly along its propagation axis $\hat{z}$ on the scale of its wavelength and varies slowly in the x-y direction as the light propagates. Separating out the fast oscillations, the field can be written as $E(x, y, z) = u(x, y, z)e^{-ikz}$ with $k = 2\pi/\lambda$ being the wavenumber corresponding to the wavelength λ of interest. The paraxial wave equation for $u(x, y, z)$ then reads (see [8])

$$\frac{\partial^2 u(x,y,z)}{\partial x^2} + \frac{\partial^2 u(x,y,z)}{\partial y^2} - 2ik\frac{\partial u(x,y,z)}{\partial z} = 0 \tag{8.1.1}$$

and gives solutions of the type

$$u(x,y,z) = \sqrt{\frac{2}{\pi}}\frac{1}{w(z)}\exp\left[-\frac{x^2+y^2}{w^2(z)}\right]\exp\left[-ikz - ik\frac{x^2+y^2}{2R(z)} + i\psi(z)\right] \tag{8.1.2}$$

with

$$\psi(z) = \arctan(z\frac{\lambda}{\pi w_0^2}),$$

$$w(z) = w_0\sqrt{1+\left(\frac{\lambda}{\pi w_0^2}z\right)^2},$$

and

$$R(z) = z + \left(\frac{\pi w_0^2}{\lambda}\right)^2 \Big/ z$$

further described below[1]. Equation (8.1.2) has a real amplitude part and an imaginary phase part.

The real part appears in the intensity as

$$I(r,z) = |E(x,y,z)|^2 = \frac{2P}{\pi w^2(z)} e^{-2(r/w(z))^2} \tag{8.1.3}$$

where $x^2 + y^2 = r^2$ (since the problem is radially symmetric) and the normalization $P = \int\int |E(x,y,z)|^2 dA$ was chosen as the total power contained in a beam at position z, which stays constant of course. One can clearly see, that $w(z)$ takes the role of the "width" of this Gaussian intensity distribution. Not surprisingly, the radius of a Gaussian beam at a position z_0 is then usually defined as the distance $r = w(z)$ for which the intensity has dropped by $1/e^2$ (see Figure 8.1.1). For a detailed derivation of the form of $w(z)$ see [8], so

$$w(z) = w_0\sqrt{1+\left(\frac{\lambda}{\pi w_0^2}z\right)^2} \tag{8.1.4}$$

is simply defined, with w_0 being the beam radius at the focus (for simplicity usually $z = 0$), also called the waist of the beam. Note that $I(r,z)$ decays like a Gaussian in the radial direction (and like a Lorentzian in the z-propagation direction). This is what gives the Gaussian beam its name.

Next is analyzed the imaginary part of eq. (8.1.2). The first two terms show the close relation of a Gaussian beam to a spherical wave. In the paraxial approximation, the amplitude of a spherical wave propagating along $\hat{\mathbf{z}}$ at distance R from the origin is proportional to $\frac{1}{R}\exp(-ikz)\exp(-ikr^2/2R)$. The similarity to the Gaussian beam is striking and $R(z)$ is defined as the radius of curvature of the wavefront on the propagation axis. Closer analysis reveals that it can be written as

$$R(z) = z + \frac{\left(\frac{\pi w_0^2}{\lambda}\right)^2}{z}. \tag{8.1.5}$$

The $\psi(z)$ term is more complicated since it takes into account the non-linear nature of the Gaussian beam solution. It describes the phase shift of π, the on-axis wavefront acquires during free propagation from $-\infty$ through the focus to $+\infty$. It is known as the Gouy phase shift and given by

$$\psi(z) = \arctan(z\frac{\lambda}{\pi w_0^2}). \tag{8.1.6}$$

[1]It should be mentioned for completeness, that this is not the only type of solution. For spherical and rectangular boundary conditions, the general solution depends on Laguerre and Hermite polynomials respectively. For both cases, the lowest order solution is of Gaussian beam type similar to eq. (8.1.2).

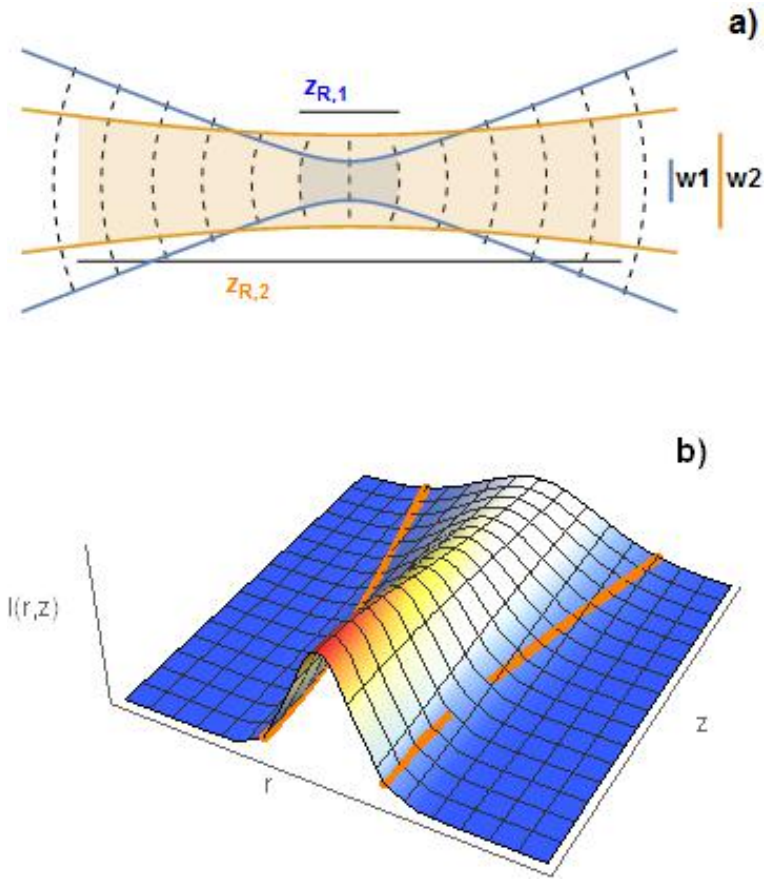

Figure 8.1.1: **a**) Sketch of two Gaussian beams with different waists. The dashed lines indicate the curvature of the wavefronts and the Rayleigh ranges are indicated. **b**) 3D sketch of a Gaussian beam with the beam radius indicated as thick orange line.

It might be surprising, but all three parameters depend only on the waist w_0 and the wavelength λ. An auxiliary parameter which has a direct physical interpretation (see Figure 8.1.1) is the Rayleigh range

$$z_R = \frac{\pi w_0^2}{\lambda}. \tag{8.1.7}$$

It indicates the propagation distance at which the beam radius has increased to $\sqrt{2}w_0$. The divergence

$$\theta = \lim_{z\to\infty} \frac{w(z)}{z} = \frac{\lambda}{\pi w_0} = \frac{w_0}{\pi^2 z_R} \tag{8.1.8}$$

is another useful characteristic of a Gaussian beam as it describes the angle between the beam radius and the propagation axis in the far field limit. As one can see, keeping the wavelength fixed leaves the waist as the only degree of freedom, so eq. (8.1.8) shows that a large waist results in smaller divergence, but a Gaussian beam can never really be collimated. On the other

hand, a very tight waist like 1 µm produces a very short Rayleigh range of around 8 µm which means that the beam diverges extremely fast. High numerical aperture (NA) lenses are then needed. The NA is defined as $n \sin\theta$, where n is the refractive index of the medium and θ the half-maximal angle of the cone of light the optical element can accept.

As a last useful quantity the spot size of the beam should be compared to the clear aperture of any optics it passes trough. Since in theory the transversal extent of the beam is infinite (but exponentially decaying), clipping will always take place. The question is, how big an aperture has to be, in order to keep this clipping below a reasonable level, say 1%. According to eq. (8.1.3), the fractional power transmitted through an aperture of radius a is

$$\frac{P}{P_0} = \frac{1}{P_0}\int_0^a I(r,\, z_0)dr = \frac{2}{\pi w^2}\int_0^a 2\pi r e^{-2r^2/w^2}dr = 1 - e^{-2a^2/w^2}. \tag{8.1.9}$$

By setting $a = \frac{1}{2}\pi w$ one can define the "99% criterion" where the aperture diameter should be π times the spot radius on the aperture in order to transmit 99% of the beam intensity. Additionally, a conservative constraint for aperture diameters reduces edge diffraction effects, which might cause problems in a string of ions.

8.2 Focusing Gaussian Beams

The most important problem of this part of the thesis is Gaussian beam focusing. Following [8], this is tackled in the far field. The Rayleigh range can be taken as the transitional region from near to "medium" field. After several Rayleigh ranges, the far field approximation holds. As mentioned before, the Rayleigh length scale for tightly focused beams can lie in the µm range, but our focusing optics are tens of mm away from the ions (see [31] for detailed numbers), so we can safely work in the far field approximation. Consider the case of a diverging beam. In the far field, the relationship between beam propagation distance and beam radius is linear:

$$w(z) = w_0\sqrt{1 + \left(\tfrac{\lambda}{\pi w_0^2} z\right)^2} \approx \tfrac{\lambda}{\pi}\tfrac{z}{w_0} \quad \text{for} \quad z \gg w_0. \tag{8.2.1}$$

If the focusing lens has a focal length f (set $z = f$ in eq. (8.2.1)) and diameter $a = \pi w/2$ (i.e. applying the 99% criterion on this lens) and using the $1/e^2$ spot size of our focused beam, then simple algebra leads to a minimal spot size

$$w_0 \approx \frac{f\lambda}{\pi a}. \tag{8.2.2}$$

The far field Gaussian beam treatment has a small, but potentially important difference to ray tracing. One has to be aware of the simple geometrical fact that the waist of a Gaussian beam will not coincide with the geometrical focus. This difference between waist and focus location is given by

$$\Delta f = \frac{z_R^2}{f} = \left(\frac{w_0}{\pi^2\theta}\right)^2 \frac{1}{f} \tag{8.2.3}$$

so the waist will always lie closer to a focusing lens than the geometric focus (see Figure 8.2.1). Is it immediately seen, that this effect is more pronounced for large Gaussian beams. This issue is worth noting, since our in-vacuum objectives were designed by Sill Optics, using ray

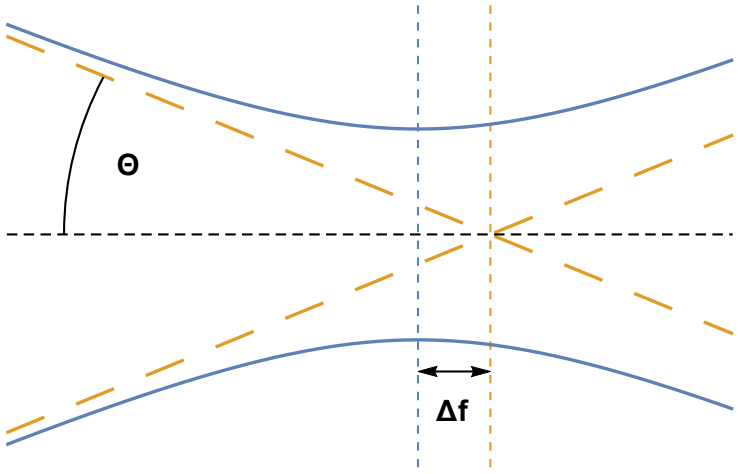

Figure 8.2.1: Location of the Gaussian waist with respect to the geometrical focus. The divergence of the beam is θ.

tracing, whereas our final simulations concerning the single-ion addressing used Gaussian beam propagation in order to estimate the light intensity at the focus.

The depth of focus is crucial for a realistic optical setup. It can simply be defined as twice the Rayleigh range and indicates on which length scale the beam intensity dropped by half of its original value. If the geometrical focus lies within the depth of focus of the focusing optics, no noticeable difference between the two models is expected.

The next section describes how these analytically approximated features of the Gaussian beam compare to the numerically simulated values and which of them might be problematic to achieve.

Chapter 9

Simulating the Single-Ion Addressing Lens System

9.1 The Imaging System

Before discussing the simulation, the pre-installed optics are introduced as a starting point. Sill Optics designed an optical system, which was installed by Dr. Hsiang-Yu Lo [31], to collect fluorescence light emitted by $^{40}Ca^{+}$ and $^{9}Be^{+}$ ions at 397 and 313 nm respectively. A cross section through the 3D model is shown in Figure 9.1.1. An in-vacuum objective nearly collimates light at both wavelengths from the same point in the focal plane. Both wavelengths are then split by a dichroic mirror. The beams are focused on CCD cameras with the help of two out-of-vacuum telescopes. The beam path of beryllium will not be of interest in this work, only the path of calcium, since only these ions will be addressed. From now on the objective and telescope will be referred to as the imaging system. Figure 9.1.1 shows the three-lens-cage system (green), as it was installed during this thesis, hopefully enabling single-ion addressing together with the pre-installed imaging system. The addressing light was sent through this new lens system and a 50/50 beam splitter[1] deflected it into the optical axis of the imaging system. The translation stage beneath the dichroic mirror (yellow) was redesigned. The next two sections describe the process of simulating the optical system for single-ion addressing in order to decide on parameters for the three-lens system. Section 10.1 explains how the imaging system was upgraded to become an addressing system.

9.2 Constraints to the Simulation

The focusing ability of the imaging system is characterized using the analytic expressions from Chapter 8. As can be seen below, the wavelengths chosen were either 397 or 401 nm light. Applying the 99% criterion from eq. (8.1.9), the objective has an effective diameter of 18 mm, so the minimal attainable waist at its focal distance (30.9 mm) is 1.3 µm. Changing the wavelength from 397 to 401 nm increases the waist only by 1%, so for simplicity the following

[1] Thorlabs BSF20-A

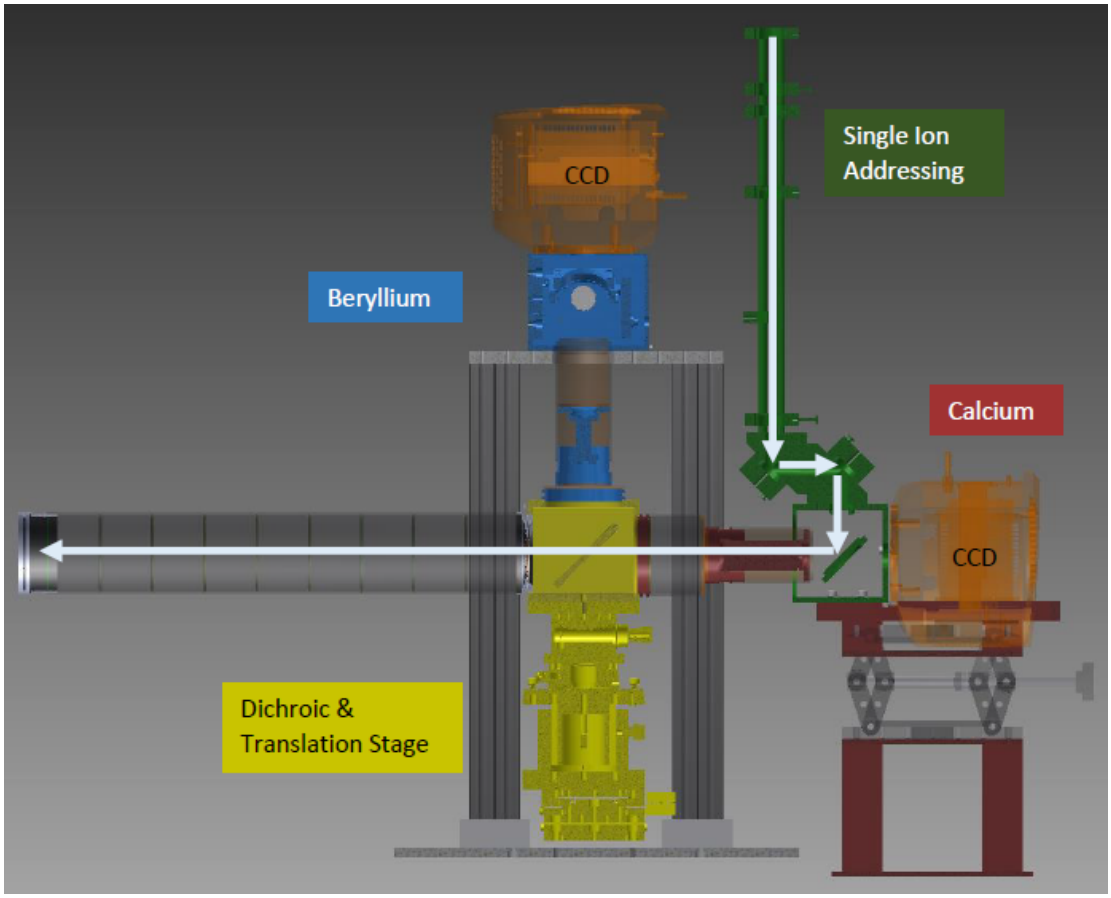

Figure 9.1.1: Cut through the imaging system with the single-ion addressing cage system added. The ion trap with the in-vacuum imaging system is to the left, and not shown. The beam path of the single-ion addressing beam is shown in white. The out-of-vacuum telescopes are fixed to the box containing the dichroic mirror.

Quantity	Expression	Value
diffraction limited beam waist	w_0	1.3 µm
wavelength	λ	397 nm
Rayleigh range	$z_R = \pi w_0^2/\lambda$	13 µm
radius of curvature	$R = z + z_R^2/z$	∞ (at the focus)
Gouy phase shift	$\psi = \arctan(z/z_R)$	0 rad (at the focus)
divergence	$\theta = \frac{w_0}{\pi^2 z_R}$	0.01 rad
99% criterion	$a = \frac{1}{2}\pi w_{\mathrm{Obj}}$	20 mm
achievable spot size	$w = f\lambda/\pi a$	0.2 µm
depth of focus	$\delta F = 2z_R$	26 µm
ray vs. Gaussian beam focus location	$\Delta f = z_R^2/f$	0.5 nm

Table 9.2.1: The Gaussian beam parameters constrained by our imaging system. Propagation distance of the beam, waist at the objective and focal length are given by z, w_{Obj} and f respectively. The other quantities are defined in Section 8. The achievable spot size is well below the diffraction limit, indicating that a diffraction limited spot should be achievable using the imaging system.

analysis is given only of 397 nm light. The Rayleigh range is then 3.7 µm leading to a very small depth of focus around 7.5 µm. The error in focal position of the ray picture is merely 0.5 nm, which is completely negligible for the achievable degree of precision. It is thus safe to work in the ray picture for the macroscopic beam path through the imaging system, as long as the beam waist after the objective is correctly calculated in the Gaussian picture. This estimation suggests, that the present imaging system is almost diffraction limited (see Section 10) and opens the possibility to achieve a waist of 1.3 µm. The small depth of focus due to the strong focusing is a physical problem one has to live with.

Table 9.2.1 summarizes the beam parameters. At the focus, the Gouy phase and the radius of curvature are 0 and ∞ respectively. The theoretically achievable waist after the objective is smaller than the waist allowed by the diffraction limit and will thus not be reached.

These conservative estimates matched our goals, so nothing fundamental was expected to hinder addressing a single trapped ion. In the following the main constraints to the simulation are discussed. The experienced reader might know that many task-specific problems arise during these kinds of projects, but it is not necessary to describe all of them in detail here. The point is to give an overview of the main difficulties of this work, as it was about upgrading a working system and not designing it from scratch.

9.2.1 Finding the Right Wavelength

In a first step, the addressing wavelength had to be chosen. For direct single-ion qubit transition addressing, the wavelength of both Raman beams had to be chosen. There is also another solution to address single ions. At the present stage, we can drive the qubit transition directly using a 729 nm laser [21] which illuminates all ions simultaneously. The idea would be to individually AC-Stark shift the resonance of a single-ion away from the qubit transition using a tightly focussed laser beam. We thus "switch on" single-ions by shining another, tightly focused laser beam on them (see Section 7.2). Light which is red detuned from a transition "pushes" the

energy levels together, blue detuned light "pulls" them apart. This form of single ion addressing will be used as long as the qubit transition still lies at 729 nm.

This procedure has one drawback. Since we discern our qubit state by the number of collected 397 nm fluorescence photons, parasitic scattering from this transition would give misleading results. A red detuned AC-Stark wavelength of 401 nm promised the smallest scattering rate (calculations performed by Dr. Hsiang-Yu Lo) and at the same time high enough Raman transition rates. The intuitive reason is the following: A blue detuned Stark-laser would bring the ion into a virtual state between $^2P_{1/2}$ and $^2P_{3/2}$ (see Figure 7.2.1). Both of these levels would contribute to unwanted parasitic scattering. On the other hand, if the Stark-laser is red detuned, only the $^2P_{1/2}$ level will contribute significantly to the scattering. A 401 nm laser[2] with more than enough power is readily available to us, as opposed to shorter wavelengths which might allow for higher Raman transition rates. Shining a strong 401 nm beam on the 397 nm transition also shifts the $|\downarrow\rangle$ qubit ground state away from resonance with the 397 nm fluorescence transition.

9.2.2 Funding

After finding an appropriate wavelength, simulations focused primarily on upgrading the imaging system with a single custom-made lens. After having found several possible designs, lens making companies either told us that such designs were impossible to manufacture (the lens would for example have to be too thin to polish) or would cost CHF 9000 upwards. We thus had to turn our focus to commercially available lenses (mainly from Thorlabs).

9.2.3 Staying Flexible

A third constraint was the ability of the upgrading system to focus two wavelengths. As main objective the 401 nm Raman beams and the AC-Stark shifting beam should be focused. But for testing purposes the setup should also be able to focus 397 nm light, for which we could easily test single ion fluorescence. We decided to opt for a cage system, in which all lenses were fixed except for one, which can be adjusted in position depending on the wavelength.

9.2.4 Physical Parameters of the Imaging System

Last but not least, the physical properties of the imaging system have to be taken into account. The most important constraint regarding the physical dimensions was that the final lens could not be too close to the imaging system telescope. As mentioned before and shown in Figure 9.1.1, a beam splitter brings the addressing beam on the optical axis of the imaging system. This dichroic is placed in a box and needs space. In the beam path this corresponds to at least 220 mm. Other dimensional constraints also had to be taken into account but were more easily met. The location focal point of the addressing beam had to stay inside the depth of focus of the imaging system objective (roughly $\pm$ 7.5 µm with respect to the image plane of the objective), the 99% criterion of eq. (8.1.9) should be fulfilled at every surface (mostly to avoid diffraction), the incoupled beam must have a realistic radius and of course, the added lenses must have realistic spacings (cage systems up to 400 mm can be considered stable).

[2] Toptica DL Pro

These constraints were challenging to meet all at once. On the other hand, they reduced the parameter space considerably. The next section explains how the simulations led to a potentially satisfactory design, using the powerful optimization algorithms of ZEMAX.

9.3 Performing the Numerical Simulation

The numerical simulation of the Gaussian beam propagation was performed in the optical design program ZEMAX. The Physical Optics Propagation package calculated the beam propagation coherently over the whole length of the optical system. With this package, aberrations like coma could also be simulated. This was not possible quantitatively using the standard Paraxial Gaussian Beam package in ZEMAX (it only gave qualitative results as the ray-tracing spot diagram was not precise enough).

As mentioned above, at the beginning of the simulations single custom lenses were investigated. These custom lenses led to decent results, so the beam path was reproduced approximately with two or three commercially available lenses in a black box model. Simple ray ABCD matrix multiplication was used to find a combination of lenses that create a path similar to a well focused one originating from a custom lens. We chose among the A-coated 1" N-BK7 and Fused Silica lenses offered by Thorlabs. Promising combinations were then implemented into ZEMAX and their relative locations were optimized with the built-in optimization algorithm. Since the parameter space was huge, it took some trial and error to get to reasonable setups.

The hardest constraint to meet was the flexibility constraint. Setups that looked promising for one wavelength failed for another. The spot size could not be small enough for both wavelengths, or it required unrealistic spacings between the lenses. The setups were extremely sensitive to all parameters because the aimed spot size was so small. Tiny changes could easily lead to beam waists 5 or 10 times the desired 1.3 µm waist.

Even when the design process took a lot of iterations, three basic principles served as a guide line:

- The beam dimensions did not change much passing through the out of vacuum optics (roughly by 10 mm over a length of 1 m), so the paraxial approximation holds. This in turn means that lens effects (like spherical aberration) should not play a major role. This rules out the necessity of for e.g. achromatic doublets or aspheric lenses and reduces the amount of lenses worth considering.

- The beam size has to stay well below all aperture dimensions in its path (99 % criterion). This constrained most of the setups and goes hand in hand with the previous point.

- Telescopes make the setup flexible for different wavelengths as the beam size and the angles can be tuned finely by moving lenses. This insight came later during the simulations, but revealed itself to be crucial.

Meeting the 99% criterion, led us to the final setup presented in Figure 9.3.1. The ingoing laser light exits a collimator[3] of a single-mode fiber[4], is contracted by a first Galilean type telescope (plano-convex and plano-concave lens with focal distances 125 mm and -100 mm respectively),

[3] Thorlabs TC12FC-405
[4] Schäfter+Kirchhoff PMC-401Si

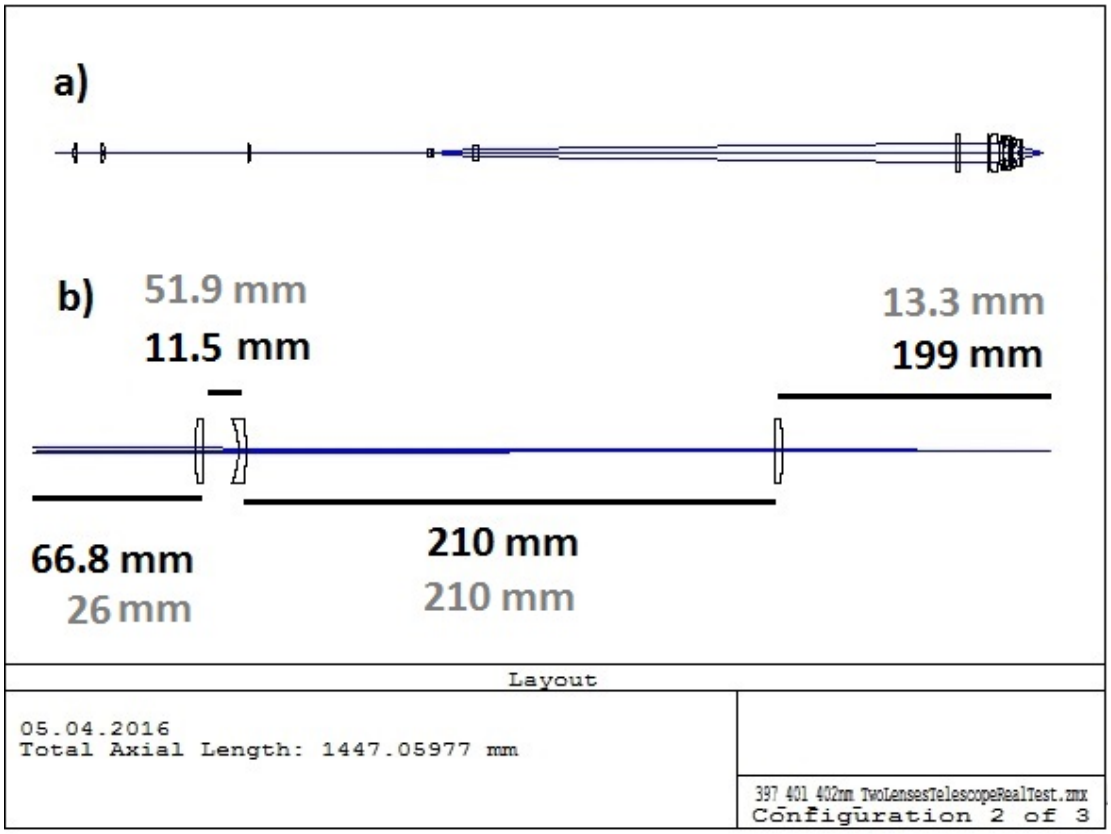

Figure 9.3.1: **a**) Sketch of the complete single-ion addressing lens system. **b**) Zoom on the three lens system developed in this project. The black numbers describe the setup for 397 nm light and the gray numbers the setup for 401 nm light. The distance to the imaging system telescope is 260 mm for both wavelengths. Note the big difference in focal length between the 397 nm and the 401 nm setup.

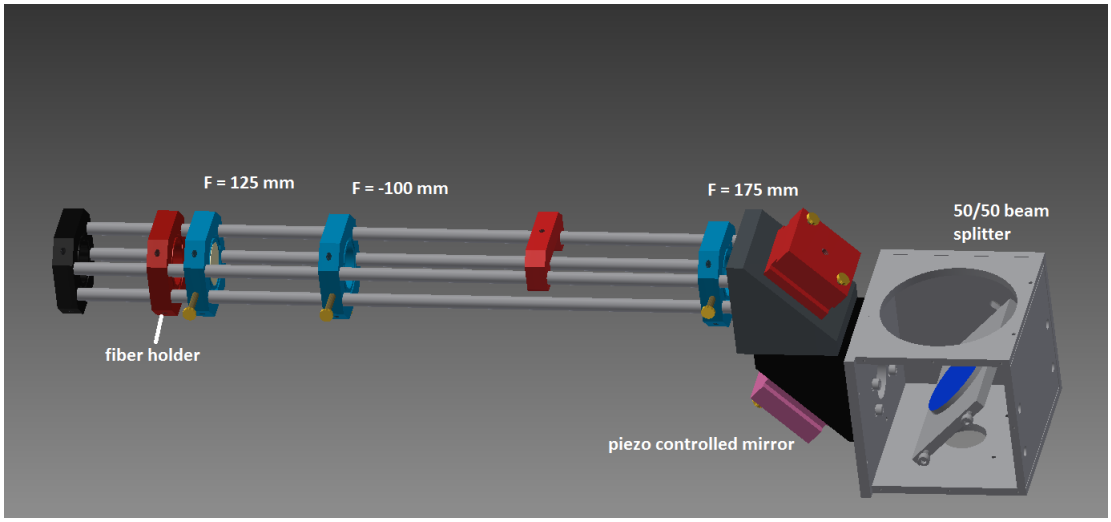

Figure 9.3.2: Cage system for the single-ion addressing three-lens system. The focal distances of the lenses are indicated. The rods are 401 mm long. Working distance is 106.5 mm for a lens diameter of 1 inch.

focused by a third lens[5] (plano-convex with focal distance 175 mm) and left expanding again until hitting the telescope of the imaging system. Finally, the objective focuses the light down to a waist around 1.3 µm. The focal length of this three-lens-telescope is 106.5 mm and has an F/# of 4.2. In theory, this system is extremely promising due to several reasons:

1. The addressing beam originates directly from a fiber with its corresponding collimator.
2. The system has a stable focal minimum, meaning that even if the spacing between two lenses is off by several mm, the third lens can always be adjusted to find a spot size around 1µm.
3. Going from 397 to 401 nm simply requires changing the distance between the first two lenses
4. The total cost of the three lenses is less than CHF 100.

These four points make it the ideal prototype to examine the possibility of single-ion addressing with our pre-installed imaging system. Of course, this setup has some drawbacks:

1. The collimator might introduce aberrations.
2. The first lens is placed 250 to 300 mm in front of the third lens, and together with the fiber holder pushes the length of the cage system to its stability limit.

Hoping that these two drawbacks were not unsurmountable difficulties, the three lenses were fixed in a cage system[6]. Figure 9.3.2 shows the cage system together with the box containing the

[5] Thorlabs LA1986-A, LC1120-A and LA1229-A
[6] Radiant Dyes

50/50 beam splitter. The box from the imaging system was redesigned in order to accommodate the beam splitter and support the cage system with four stabilizing pin holder. One of the two mirrors coupling the beam onto the optical axis of the imaging system could be controlled precisely with piezos on each rotation axis.

Chapter 10

Experimental Setup and Test

10.1 Aligning the Imaging System for Reverse Operation

As the name suggests, the imaging system collects light from inside the ion trap and images the ion on a camera or a photon counter outside. In the simulated single-ion addressing, light is sent through three lenses in front of the imaging system, and then through the whole imaging system into the ion trap. This means, that the imaging system is used in both directions: for imaging and addressing ions. Prior to my work on the system, the images of the ions showed considerable coma. Figure 10.1.1 shows trapped ions with a tail, resembling the one of a comet. Coma, or comatic aberration, originates from light rays hitting lenses (or any optical element) at an angle. A circular image gets a comet-like tail (see Figure 10.1.1 a)). Light propagating through the system in the reverse direction will be focused to an equally comatic spot, with the comet-tail pointing in the opposite direction. Depending on the severity of the coma, a lot of light might be transferred to the tail. Single-ion addressing with coma in the system is not ideal, as neighboring ions could be illuminated too much by the distorted laser spot. One appealing feature of the design discussed in the previous section was that it used the whole imaging system, so it forced us to first correct the coma before we could proceed to addressing single-ions.

Based on the separation between the ions in Figure 10.1.1 being roughly 3.5 µm the amount of coma present in the system could be estimated. Using Physical Optics in ZEMAX the presented shape was approximated and the closest result is shown in Figure 10.1.1 b). We could estimate a tilt of roughly 1.75 degree in the objective and no significant displacement of either the objective or the telescope. Already a slight tilt in the telescope led to a much more sickle-shaped form of the coma, so it was concluded that the main contribution to coma came from the tilted objective.

With this information at hand the translation stages beneath the 313/397 nm dichroic (see Figure 10.1.2) was redesigned. After installing an additional goniometer[1] for vertical tilting and a rotation stage[2], the coma could almost entirely be corrected. A string of ions can be see in Figure 10.1.3 a). An Airy pattern and a Gaussian fit to the data is shown in Figure 10.1.3 b). Both are nearly indistinguishable and have almost the same relative errors. Also shown are

[1] Owis GO90
[2] Thorlabs PR01/M

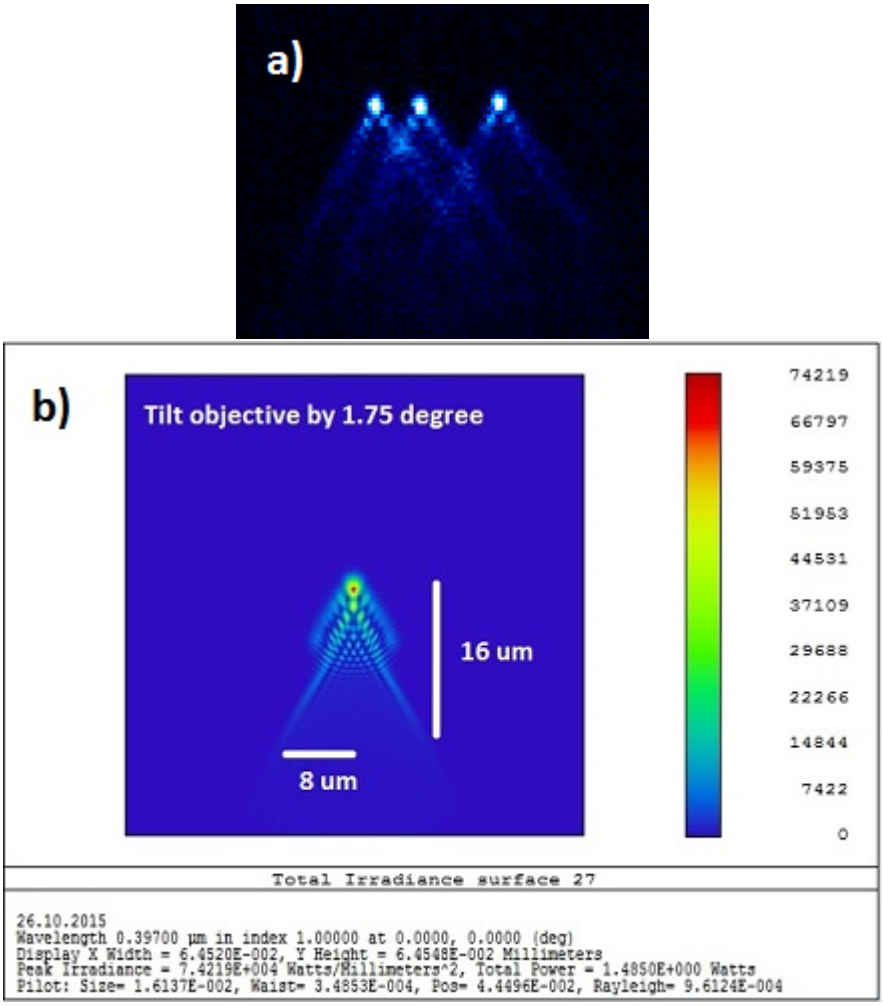

Figure 10.1.1: **a**) Trapped ions exhibiting comatic aberration. **b**) Simulation of the imaging system coma using ZEMAX. The separation between the ions in **a**), estimated around 5 µm, served as a rough scale and led to approximate the tilt of the objective between 1° and 2°.

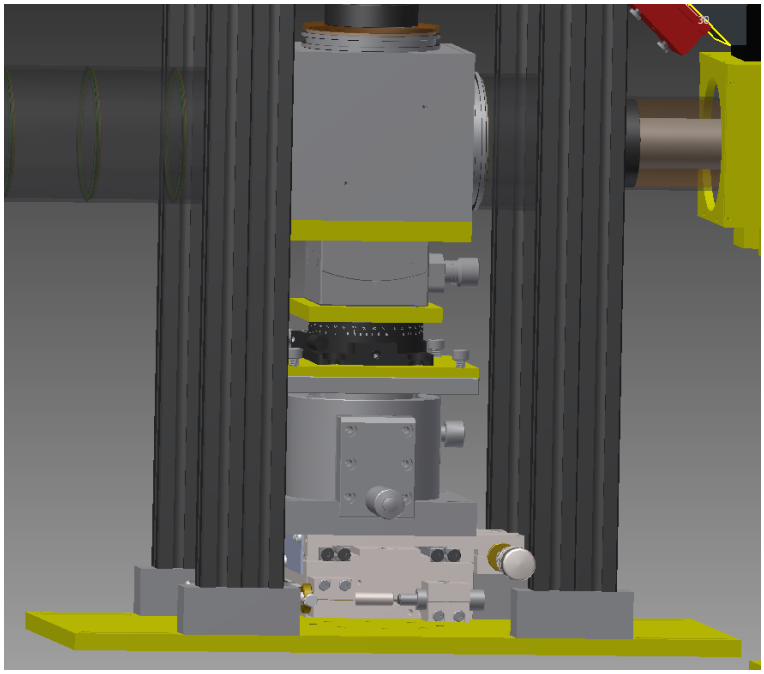

Figure 10.1.2: The upgraded translation stage. The adapter plates shown in yellow had to be manufactured by the workshop.

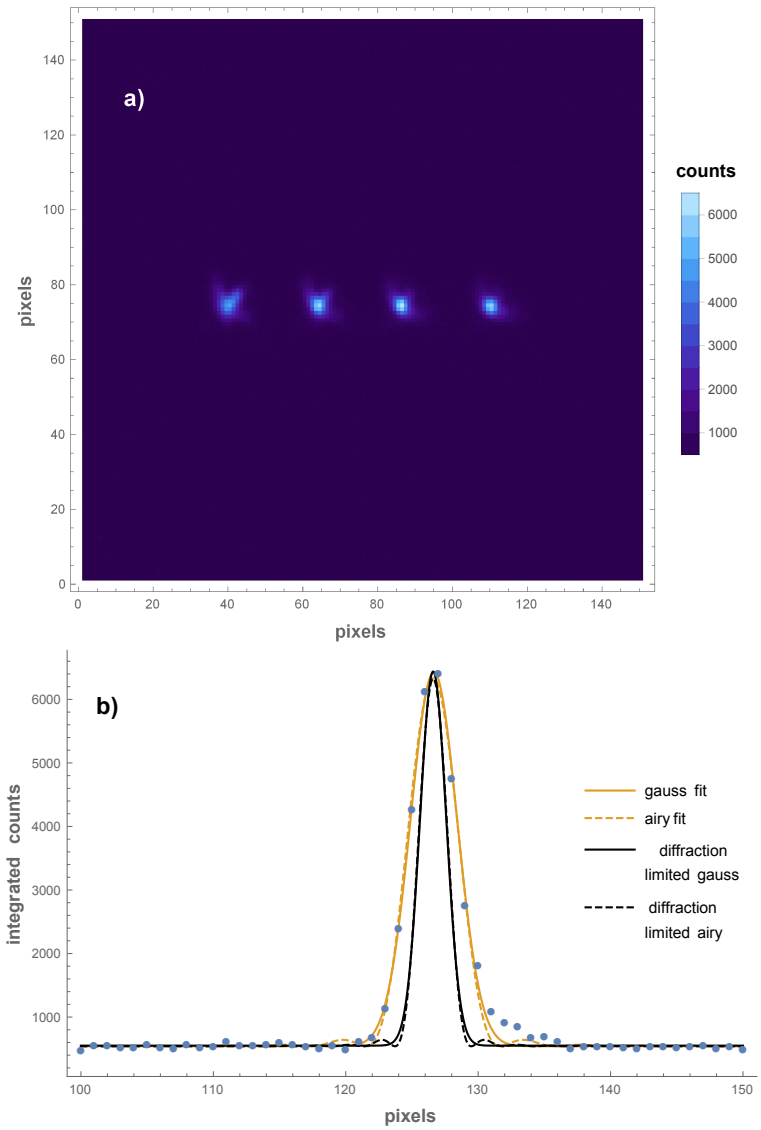

Figure 10.1.3: **a**) Four trapped $^{40}Ca^{+}$ ions after coma correction. The second ion from the right is the sharpest and brightest due to residual coma in the imaging system. **b**) Airy as well as Gaussian fit to a single trapped ion. The diffraction limited Airy and gauss function are also shown.

the Airy pattern and its Gaussian approximate for the diffraction limited case. The Rayleigh criterion states that two spots can be resolved, if the peak of one Airy pattern coincides with the first zero of the other (see [37]). For an aperture of diameter d the minimal angular separation of the two spots is then given by Abbe's criterion as

$$\sin\theta \approx 1.22\frac{\lambda}{d} \tag{10.1.1}$$

where λ is the wavelength of the imaging light. If f is the focal length of the imaging system and x the minimal distance between the two spots we can also formulate 10.1.1 with the help of the f-number $F/\# = \frac{f}{d}$ of the imaging system as

$$x \approx 1.22\lambda F/\# = 1.22 \cdot 397\,\text{nm}\,1.1 = 0.53\,\mu\text{m} \tag{10.1.2}$$

in our case (see [31]). Approximating the Airy function with a Gaussian of the same height, yields for its standard deviation

$$\sigma \approx 0.42\lambda F/\# = 0.18\,\mu\text{m}. \tag{10.1.3}$$

The imaging system has a magnification of 40 and the CCD camera[3] used to monitor the ions has a pixel size of 7.4 µm. The diffraction-limited spot should then be about 6 pixels wide opposed to the recorded spot which was roughly 10 pixel wide. The imaging system is therefore near diffraction limited. The small discrepancy might be explained either by a slight defocus or the coma being reduced, but not entirely corrected now manifesting itself in a complicate pattern broadening the spot.

10.2 Addressing a Single Ion

Having aligned the imaging system very well, the addressing beam was sent through to the trap. In order align the beam, it was reflected on a trap-electrode and imaged on the calcium CCD camera. The objective was moved away from the ions and focused on the trap electrodes. The objective was then moved back, bringing the addressing beam roughly to the location of the ions. The CCD camera was then replaced by a photo multiplier tube (PMT), monitoring the fluorescence of the ions. The ideal case would have been to shine 15 mW with a beam waist of 1.3 µm on the ions. From eq. (7.3.2) an AC-Stark shift up to 800 MHz can be achieved in this case. Ion fluorescence would then completely be inhibited.

In the real setup however, the 50/50 beam splitter allowed too much scattering light to hit the PMT. The imaging telescope reflected part of the addressing beam back to the beam splitter (see Figure 10.2.1). Half of this reflection was reflected again, the other half transmitted directly onto the PMT. Already for an AC-Stark beam power around 1 µW the photon number fluctuation was bigger than the fluorescence count. Less than half of this power is available at the ion location (because of the 50/50 beam splitter and the reflection at the telescope). Therefore even at a minimal waist of 1.3 µm, an AC-Stark shift of only 5 KHz is induced. As the 397 nm fluorescence transition linewidth is around 20 MHz wide, a drop in fluorescence counts is almost impossible to detect.

[3] QSI RS 4.2

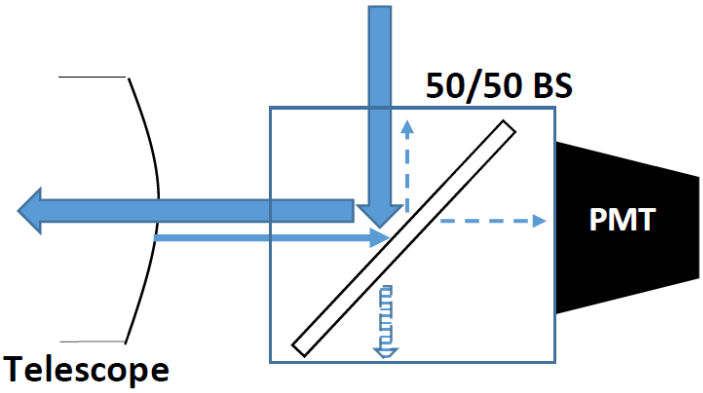

Figure 10.2.1: Single ion addressing beam reflected off the telescope and transmitted by the 50/50 beam splitter (BS) into to photomultiplier tube (PMT).

The 50/50 beam splitter limited the amount of power we were able to use in order to AC-Stark shift the ions away from their fluorescence transition. A dichroic mirror reflecting 401 nm and transmitting 397 nm should solve this problem. Even if light is reflected from the telescope, the dichroic mirror will reflect it away from the PMT, transmitting only the fluorescence light of the ions. The power of the single ion addressing beam can then be increased.

Chapter 11

Conclusion and Outlook

In this project a preexisting imaging system for trapped $^{40}Ca^{+}$ ions was upgraded for the reverse usage of single ion addressing. Simulations were performed and a prototype was set up. The system is designed to shape beams with wavelengths between 397 and 405 nm which are then focused below 1.3 µm beam waist by the imaging system. Such great flexibility is achieved by designing an additional three-lens-telescope. For shorter wavelengths the spacing between lenses gets too low, whereas for longer wavelengths the spacing gets too large to build a stable mechanical support for the lenses. All three lenses are commercially available, cheap and the ion addressing beam can be sent directly out of a fiber-collimator through the setup.

In addition, the preexisting imaging system was coma-corrected and confirmed to be near-diffraction limited. Additional rotation and tilting stages were installed beneath the imaging system, to enable almost perfect imaging of trapped ions. This correction also had to be made in order to keep a Gaussian profile of the single ion addressing beam at the location of the ions.

Single ion addressing with this system is yet to be confirmed in the lab. In a first run, single ions could not be AC-Stark shifted away from their fluorescence transition because a simple 50/50 beam splitter allowed too much scattering light to hit the photo multiplier tube. As a "hardware-solution" to this problem a dichroic mirror transmitting 397 nm and reflecting 401 nm might be installed. Reflected light should then be completely suppressed. Two other solutions use the properties of atomic transitions in $^{40}Ca^{+}$ in order to reduce the power of the addressing beam. The first possibility uses ion shelving. As we mentioned earlier, approximately one in ten photons decays from the $P_{1/2}$ state to the $D_{3/2}$ state. This means that after only roughly ten photons, the Calcium ion is in a dark state, non-responding to fluorescence. At such low powers single ion addressing could be probed with very low background. The second possibility makes use of a very narrow linewidth transition in $^{40}Ca^{+}$. Shifting the 729 nm $S_{1/2} \rightarrow D_{5/2}$ transition could be probed with very little power as the linewidth of thsi transition is just several 100 Hz. Significant AC-Stark shift could then be observed at very low powers.

Once single ion addressing has been demonstrated by one of these methods, two co-propagating Raman beams will be focused on a single ion to drive the Zeeman qubit transition in $^{40}Ca^{+}$ selectively. Individually addressed single qubit gate manipulation will then be possible in the TIQI lab.

Bibliography

[1] M. Gulley, et al., "A Raman approach to quantum logic in Calcium-like ions", arXiv:quant-ph/0112117, 2001.

[2] E. Lau, "High-Speed Modulation of Optical Injection-Locked Semiconductor Lasers", PhD thesis, UC Berkley, 2006.

[3] A. Pikovsky, "Synchronization-A Universal Concept in Nonlinear Science", Cam. Univ. Press, 2001.

[4] F. Leupold, "Bang-bang Control of a Trapped-Ion Oscillator", PhD thesis, ETH Zürich, 2015.

[5] M. Sepiol, "Stabilization of a 729 nm laser to an ultra-high finesse reference cavity", Master's Thesis, ETH Zürich, 2012.

[6] L. Gerster,"Spectral filtering and laser diode injection for multi-qubit trapped ion gates", Master's Thesis, ETH Zürich, 2015.

[7] V.M. Schäfer, et al., "Optical injection and spectral filtering of high-power ultraviolet laser diodes", Opt. Lett., vol. 40, pp. 4265-4268, 2015.

[8] A.Siegmann, "Lasers", C. Mill Valley, Ed. Univ. Sc. Books, 1986.

[9] N. Lanka, et al., "Understanding the Transient Behavior of Injection Locked LC Oscillators", IEEE CICC, pp. 667–670, 2007.

[10] B. Razavi, "A Study of Injection Locking and Pulling in Oscillators", IEEE J. Solid-State Circuits, vol. 39, pp.1415-1424, Sept. 2004.

[11] R. Adler, "A Study of Locking Phenomena in Oscillators", Proc. IEEE, vol. 61, pp. 1380-1385, Oct. 1973.

[12] R. H. Pantell, "The Laser Oscillator with an External Signal", Proc. IEEE, vol. 53, pp. 474-477, Oct. 1965.

[13] M. Kristić, "Statical and Dynamical Characteristics of Injection-Locked Fabry-Pérot Laser Diodes", PhD thesis, Univ. Belgrad, 2015.

[14] R. Hui, et al. , "Dynamics of optically switched bistable laser diodes in the injection-locked state", Opt. Lett., vol. 18, no. 20, pp. 1733-1735, 1993.

[15] M. Marinelli, "High Finesse Cavity for Optical Trapping of Ions", Master's Thesis, ETH Zürich, 2015.

[16] K. Balakier, et al., "Optical injection locking of monolithically integrated photonic source for generation of high purity signals above 100 GHz", Opt. Express, vol. 22, no. 24, pp. 29404-29412, 2014.

[17] G. Stein, "Respect the Unstable", Bode lecture, 2003.

[18] J. Benhelm, "Towards fault-tolerant quantum computing with trapped ions", Nature Phys. 4, 463 - 466, 2008.

[19] P. Bhansali, et al., "Gen-Adler: the Generalized Adler's equation for injection locking analysis in oscillators", IEEE ASP-DAC, pp. 522-527, 2009.

[20] L. de Clercq, et al., "Parallel Transport Quantum Logic Gates with Trapped Ions", Phys. Rev. Lett. 116, 080502, 2016.

[21] H. C. Nägerl, et al., "Laser addressing of individual ions in a linear ion trap", Phys. Rev. A 60, 145, 1999.

[22] D. Kienzler, "Quantum Harmonic State Synthesis by Reservoir Engineering", PhD thesis, ETH Zürich, 2015.

[23] F. Lindenfelser, et al. "Quantum control of the motional states of trapped ions through fast switching of trapping potentials", Rev. Sci. Instrum. 86, 033107, 2015.

[24] M. Nielsen, et al., "Quantum Computation and Quantum Information", Cam. Univ. Press, 2011.

[25] D. Gottesmann, "The Heisenberg Representation of Quantum Computers", arXiv:quant-ph/9807006, 1998.

[26] M. Hall, et al., "Ultrafast Switching of Photonic Entanglement", Phys. Rev. Lett. 106, 053901, 2011.

[27] W. Gao, et al., "Observation of entanglement between a quantum dot spin and a single photon", Nature 491, 426-430, 2012.

[28] M. Devoret, et al., "Superconducting Qubits: A Short Review", arXiv:cond-mat/0411174, 2004.

[29] D. Wineland, et al., "Experimental Issues in Coherent Quantum-State Manipulation of Trapped Atomic Ions", J. Res. Natl. Inst. Stand. Technol. 103, 259, 1998.

[30] H. Haken, et al., "Atomic and Quantum Physics", Springer, 1987.

[31] H-Y. Lo, "Creation of Squeezed Schrödinger's Cat States in a Mixed-Species Ion Trap", PhD Thesis, ETH Zürich, 2015.

[32] D. Leibfried, et al. "Quantum dynamics of single trapped ions", Rev. Mod. Phys. 75, pp. 281-324, 2003.

[33] D. Steck, "Quantum and Atom Optics", http://atomoptics-nas.uoregon.edu/~dsteck/teaching/quantum-optics/quantum-optics-notes.pdf, Lecture Notes, 2015.

[34] B. King, "Angular Momentum Coupling and Rabi Frequencies for Simple Atomic Transitions", arXiv:0804.4528, 2008.

[35] B. Keitch, "A Quantum Memory Qubit in Calcium-43", PhD Thesis, Univ. Oxford, 2007.

[36] C. Decaroli, "Optical Design for Addressing of Single Ions in a 3-D Paul Trap", Semester thesis, ETH Zürich, 2015.

[37] E. Hecht, "Optics-Fourth Edition", Pearson Ed. Unlim., 2014.

[38] K. Mobarhan, "Test and Characterization of Laser Diodes: Determination of Principal Parameters", App. Note Newport, 1999.

Appendix A

Analytical Solution of Adler's Equation

Adler's original analytical solution to his equation

$$\frac{d\phi(t)}{dt} = (\omega_{free} - \omega_{inj}) - \omega_R \sin(\phi(t)) \tag{A.0.1}$$

is very brief and rarely derived in the literature. Adler's solution is somewhat complicated, and in the main step, extremely short. This appendix shows a simple way of solving this differential equation for frequencies $|\omega_{free} - \omega_{inj}| < \omega_R$ inside the locking range.

The main trick is the substitution

$$\sin\left(\frac{\phi(t)}{2}\right) = u(t) \tag{A.0.2}$$

which leads us to $\sin\phi = \frac{2u}{u^2+1}$, $\cos\phi = \frac{u^2-1}{u^2+1}$ and for the differential

$$\frac{d\phi}{dt} = \frac{d\phi}{du}\frac{du}{dt} = \frac{2}{u^2+1}\frac{du}{dt}. \tag{A.0.3}$$

We suppress the time dependence for clarity. Plugging eq. (A.0.3) into eq. (A.0.1) yields the new differential equation for $u(t)$ as

$$\frac{du}{dt} = (\omega_{free} - \omega_{inj})\frac{u^2+1}{2} - \omega_R u \tag{A.0.4}$$

which after completing the square we can reformulate as

$$\frac{du}{dt} = \left(\sqrt{\frac{\omega_{free} - \omega_{inj}}{2}}u - \frac{\omega_R}{\sqrt{2(\omega_{free} - \omega_{inj})}}\right)^2 + \frac{(\omega_{free} - \omega_{inj})^2 - \omega_R^2}{2(\omega_{free} - \omega_{inj})}. \tag{A.0.5}$$

We substitute $y \equiv \sqrt{\frac{\omega_{free}-\omega_{inj}}{2}}u - \frac{\omega_R}{\sqrt{2(\omega_{free}-\omega_{inj})}}$. Note that $du = \sqrt{\frac{2}{\omega_{free}-\omega_{inj}}}dy$ and we get

$$\frac{dy}{dt} = \sqrt{\frac{\omega_{free} - \omega_{inj}}{2}}y^2 + \sqrt{\frac{\omega_{free} - \omega_{inj}}{2}}\frac{(\omega_{free} - \omega_{inj})^2 - \omega_R^2}{2(\omega_{free} - \omega_{inj})} \tag{A.0.6}$$

which we identify as a Riccati equation. The solution to Riccati's differential equation

$$\frac{dy}{dt} = ay^2 + by + c \tag{A.0.7}$$

is known to be

$$y = \frac{-b + \sqrt{-b^2 + 4ac}}{2a} \tan\left[\frac{1}{2}\left(\sqrt{-b^2 + 4ac}(t - t_0)\right)\right] \tag{A.0.8}$$

where t_0 is to be determined by the initial conditions. Identification of the coefficients and simplification leads us to

$$y = \frac{\sqrt{\left(\omega_{free} - \omega_{inj}\right)^2 - \omega_R^2}}{\sqrt{2\left(\omega_{free} - \omega_{inj}\right)}} \tan\left[\sqrt{\frac{\left(\omega_{free} - \omega_{inj}\right)^2 - \omega_R^2}{4}}\left(t - t_0\right)\right]. \tag{A.0.9}$$

We have to keep in mind that inside the locking range we have $\left(\omega_{free} - \omega_{inj}\right)^2 < \omega_R^2$. Thus the square-root terms are imaginary. Back-substituting u and then ϕ leads to

$$\tan\left(\frac{\phi(t) - \phi_0}{2}\right) = \frac{\omega_R}{\omega_{free} - \omega_{inj}} + \frac{i\sqrt{\omega_R^2 - \left(\omega_{free} - \omega_{inj}\right)^2}}{\omega_{free} - \omega_{inj}} \tan\left[\frac{i\sqrt{\omega_R^2 - \left(\omega_{free} - \omega_{inj}\right)^2}}{2}\left(t - t_0\right)\right] \tag{A.0.10}$$

and using the identity $\tan ix = i\tanh x$ we arrive at our final result, the well known analytical solution of Adler's equation

$$\tan\left(\frac{\phi(t) - \phi_0}{2}\right) = -\frac{\omega_R}{\omega_{inj} - \omega_{free}} + \frac{\omega_B}{\omega_{inj} - \omega_{free}} \tanh\left[\frac{\omega_B}{2}\left(t - t_0\right)\right] \tag{A.0.11}$$

where $\omega_B = \sqrt{\omega_R^2 - \left(\omega_{free} - \omega_{inj}\right)^2}$ as defined in the text.

Appendix B

Optical Output Power of the Slave Diode

Figure B.0.1 a) shows the optical output power by the slave diode at 25 °C. The curve looks extremely similar for temperatures down to 15 °C. The output power dependency of the diode on temperature is very low, suggesting a high effective temperature. Phenomenologically [38] the threshold current I_{th} depends exponentially on the temperature T, so we can write

$$I_{th} = I_0 e^{T/T_0}$$

for some constant fitting parameters I_0 and T_0. The latter is called the effective temperature and gives a rough estimate from which temperature on, the lasing threshold of the diode is significantly altered. Taking the logarithm and differentiating both sides with respect to temperature leads to

$$\frac{d \ln I_{th}}{dT} = \frac{1}{T_0}$$

where T_0 is given in Kelvin. Usually the characteristic temperature for a semiconductor laser diode lies in the range of 50-150 K [38]. Figure B.0.1 b) shows that in our case $T_{eff} = 585$ K, which indicates an extremely low sensitivity of the optical output power to temperature variation.

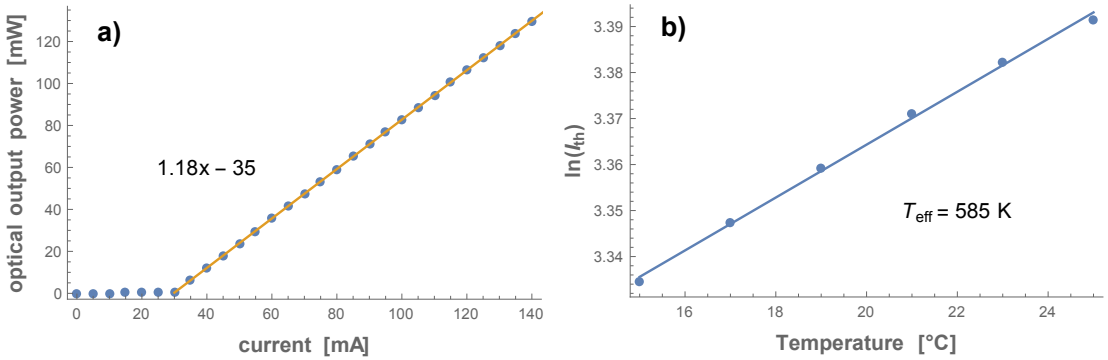

Figure B.0.1: **a**) Optical power depending on the current applied to the slave diode at 25 °C. Also shown is the expression for the linear fit. The threshold current lies around 30 mA. **b**) Natural logarithm of the threshold current I_{th} vs. temperature. The inverse of the slope of the linear fit gives the effective temperature T_{eff} of the diode.

Appendix C

Complete Injection Set Up

C.1 Optical Set Up

In this section, the optical paths in the injection setup are described. First is presented the path of the master laser. The master laser is coupled into a single mode UV fiber (SMF) to get it to the experimental zone on the optical table. In doing so, around 60 % of the light is lost. A telescope (F1 & F2) reduced the size of the beam exiting the fiber from 2.1 mm to 1 mm, for incoupling into the AOM. This step was a precautionary measure because the influence of switching the acoustic RF wave in the AOM is only well characterized if the beam size does not exceed 1 mm. The AOM was set up in a double pass configuration (lens F3). The 0^{th} order is blocked in both paths, resulting in a 80 MHz + 80 MHz = 160 MHz frequency shifted beam. The master laser is again attenuated by 50 % at this point. The $\lambda/2$ plate is used to maximize the power sent through the Fraday isolator (FI in C.1.1). Here we lose 1 % of the light. A maximal power of 50 µW was achieved for injection. We have to stress here that this was enough for injecting the laser diode and no extra effort went into maximizing the available master laser power. A small portion of the master laser was also picked off (dashed line in C.1.1) and used to create a beat note with the injected laser light in the modulation experiment. The $\lambda/2$ plate was used to match the polarization of the two beams, otherwise no interference would have been possible. Both beams were combined using a simple 50/50 beam splitter (BS). The resulting interfering light was sent onto a fast photodiode (fast PD) to detect the optical intensity beat note at 160 MHz.

The slave laser path is conceptually much simpler. Leaving the diode, the light goes through the FI and is picked off twice before hitting the grating. The first pick off leads light to the modulation experiment, whereas the second pick off (50/50 mirror) takes light to the home built optical spectrum analyzer (OSA). A $\lambda/2$ plate ensured maximal transmission through the following polarizing beamsplitter (PBS), and a $\lambda/4$ plate rotated the polarization of the reflected light such that it was reflected from the PBS onto a PD. Another PD was placed behind the OSA to monitor the transmission signal as the length of the OSA was scanned. Comparing the reflected to the transmitted signal, we were able to estimate the quality of our OSA. The waist of the slave laser was optimized for maximal incoupling into the OSA with a lens (F4). After the two pick offs, a $\lambda/2$ plate was used to match the polarization of the slave laser to the grating. A telescope (F5 & F6) expanded the beam to 3 mm diameter for better resolution

after the grating. The optimal incoming angle for maximum diffraction into the first order was 34°. Switching the RF drive of the AOM on and off (thus switching the injection) resulted in switching the wavelength of the slave, which was converted into a spatial displacement by the grating. A fast PD recorded the sharp rise time of this process. Table C.1.1 summarizes the equipment used for this setup.

lens	F1	F2	F3	F4	F5	F6
focal length [mm]	150	75	125	400	-50	150

Table C.1.1: Summary of the focal lengths of the used lenses.

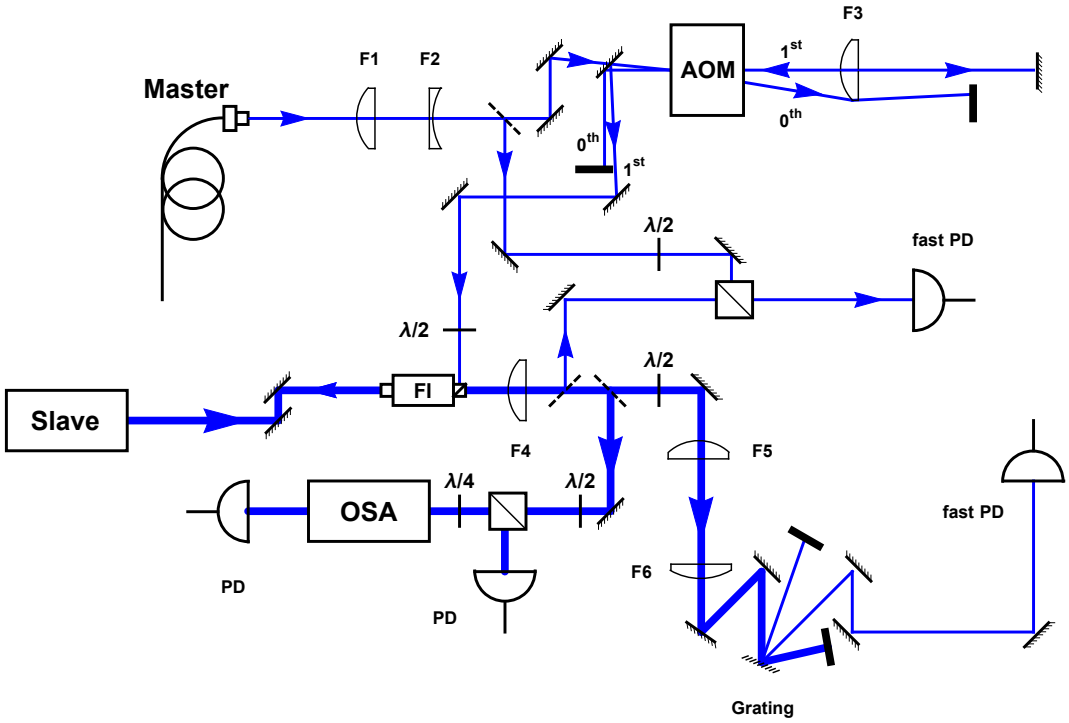

Figure C.1.1: Sketch of the complete injection set up.

C.2 Electric Control of the AOM

This section describes the material used to control the different RF signals applied to the AOM. The tunable RF source gave out the 80 MHz signal required for the AOM. The waveform generator was used in two ways. In the modulation experiment of Section 4.1, it could be used to create an amplitude modulated (AM) signal by mixing its signal with the RF signal (tunable via the amplitude and the offset of the wave form generator signal). The second use, was to

control the RF switch by applying TTL square pulses to it. A directional coupler fed all signals to a spectrum analyzer for monitoring. The RF switch, as well as the RF amplifier needed power supplies.

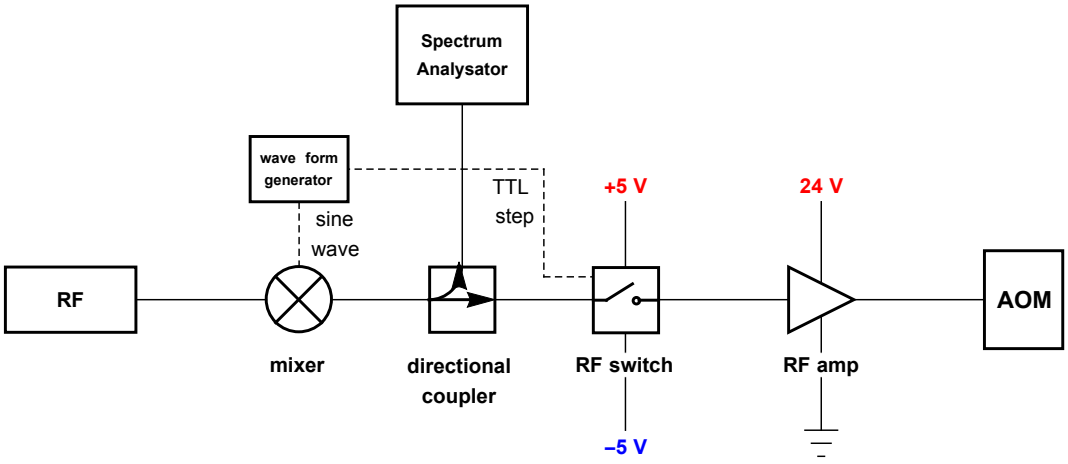

Figure C.2.1: Sketch of the electronic control of the AOM. The dashed lines indicate the two separate uses of the wave form generator.

Appendix D

AM Suppression by Optical Injection Locking

Shown is a result from [2], where the residual amplitude modulation (RAM) suppression of master AM to slave AM is shown.

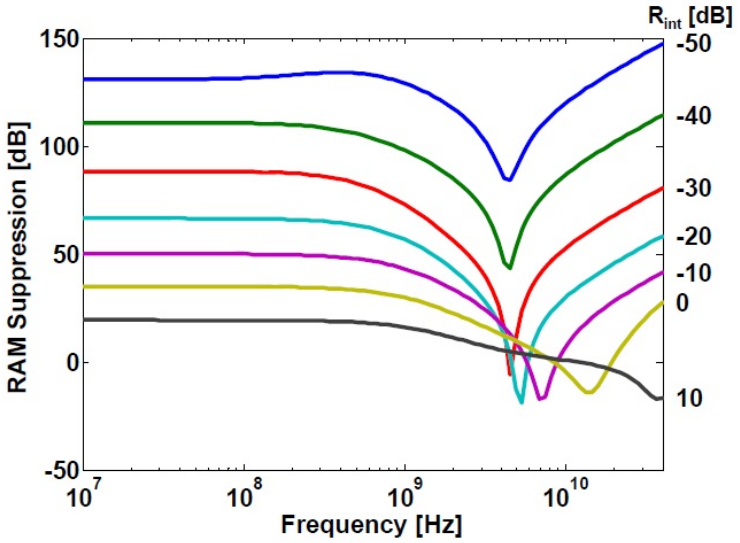

Figure D.0.1: Residual amplitude modulation (RAM) suppression for an injected 1550 nm laser diode measured by E. Lau [2]. The horizontal axis denotes the modulation frequency, R_{int} stands for the ratio between master and slave intensity I_{inj}/I_{free}. For some frequencies and R_{int}, suppression is converted into amplification.